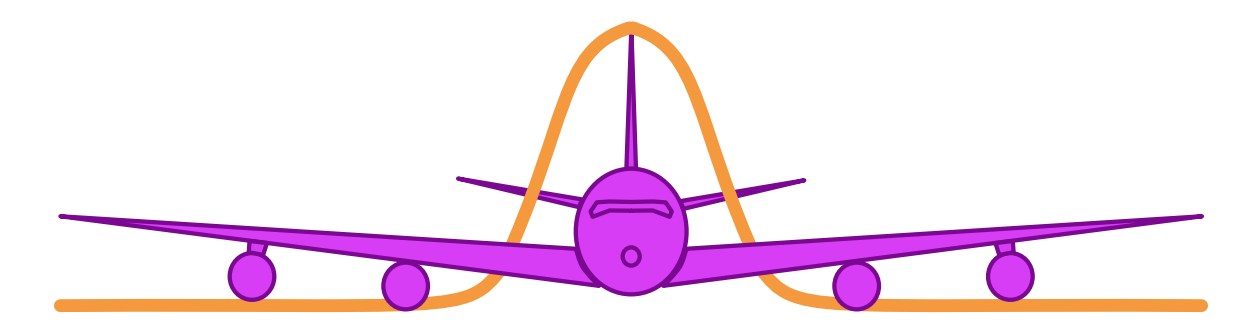
Master Thesis

University of Cologne FZ Jülich

Institute of Physics I IEK-8 Troposphäre



Quantification of Oxygenated Volatile Organic Compounds using Collision-Induced-Dissociation during the AEROMMA Campaign

November 2, 2023

Milan Roska

Primary Examiner: Prof. Dr. Hendrik Fuchs

Secondary Examiner: Prof. Dr. Stephan Schlemmer

Supervisor: Dr. Georgios Gkatzelis

A current bottleneck in accurately predicting the impacts of urban emissions on secondary pollution, including ozone and secondary organic aerosol, is the quantification of oxygenated volatile organic compounds (OVOCs). In this work, a voltage scanning (VS) method for quantifying OVOCs, utilizing collision-induced dissociation, is developed using the VOCUS chemical ionization mass spectrometer operated with ammonium as reagent ions. The method is optimized in laboratory studies and tested in the most challenging environment aboard a scientific aircraft during the AEROMMA 2023 campaign to quantify OVOCs in plumes over the Chicago metropolitan area.

Voltage scans are optimized to produce for the first time outcomes down to within a 5-second time resolution. Several OVOCs are quantified that originate from unconventional emerging pollution sources in urban air including cooking and daily household chemicals, in particular solvents and fragrances. Furthermore, the VS method is used to successfully quantify oxidation products within these emissions, notably organic nitrates, traditionally difficult to calibrate. Importantly, we determine the sensitivity of a prevalent organic nitrate in urban air, laying the foundation for refining chemical transport models. This study therefore demonstrates the voltage scanning method's versatility and effectiveness in quantifying complex compounds during field measurements, particularly in urban environments.

List of Abbreviations

PM_{2.5} Particulate Matter with diameterless then 2.5 μ m

POA Primary Organic Aerosol
SOA Secondary Organic Aerosol
VOC Volatile Organic Compound

OVOC Oxygenated Volatile Organic Compound

MS Mass Spectrometer
CI Chemical Ionization

PTR Proton Transfer Reaction

VOCUS Instrument name

IMR Ion-Molecular-Rreactor
BSQ Big-Segmented-Quadrupole

TOF Time of Flight Mass Discriminator

LTOF long Time of Flight Mass Discriminator

MCP Multichannel Plate

VS Voltage Scan

FZJ Forschungszentrum Jülich

IEK-8 Institut für Energie- und Klimaforschung (Troposphäre)
NOAA National Oceanic and Atmospheric Administration
NASA National Aeronautics and Space Administration
AEROMMA Atmospheric Emissions and Reactions Observed

from Megacities to Marine Areas

CDS Counts per Second

ppb/ppt Parts per Billion/Trillion
MVK Methyl vinyl ketone

PGMEA Propylene glycol methyl ether acetate

UTC Coordinated Universal Time
CDT North American Central Time

Contents

1.	Intro	oduction	2
	1.1.	Air Quality and Climate Change	2
	1.2.	Changing Emissions of our Complex Environment	3
	1.3.	Instrumentation used for Emission Measurement	5
	1.4.	Advances in Mass Spectrometry	8
2.	Aim	s and Objectives	10
3.	Inst	rument Characterization and Optimization	11
	3.1.	VOCUS Principle of Operation	11
	3.2.	Minimizing Discharges in the Ion Source	17
	3.3.	Optimization of the Primary Reagent Ions Distribution	19
	3.4.	Ionization Pathways	20
4.	Met	hod Development	23
	4.1.	Development of Standard Operating Procedure for Calibration and	
		Field Measurements	23
	4.2.	Collision Induced Dissociation to estimate Instrument Sensitivities	25
		4.2.1. Kinetic Energies of Ion Clusters in electrical Field	26
		4.2.2. Implementation and Scripting	28
		4.2.3. Estimation of the Kinetic energy at half decayed Signal	29
		4.2.4. Correlating Result to calibrated Sensitivities	32
		4.2.5. Error Propagation and Uncertainties of the VS Method	33
		4.2.6. Declustering into lower Order Clusters	35
		4.2.7. Voltage Scanning Optimization	36
5.	lmp	lementation of Voltage Scanning during AEROMMA Campaign	39
	5.1.	AEROMMA Flight over the Chicago metropolitan Area	40
	5.2.	Quantification of Ethylene Glycol Concentrations using the VS Method	43
	5.3	Quantification of Key oxygenated Compounds in urban Plumes	49

Contents

6.	Conclusions and Outlook	52
Bi	bliography	55
Α.	Appendix	A 2
	A.1. Instrument Background	A 2
	A.2. Instrument Comparison	А 3
	A.3. Calibration results	A 4
	A.4. Error Propagation of Conversion to Kinetic Energie	A 5
	A.5. Lag of written Voltage Values	A 6
	A.6. Calculation of Coefficient of Determination for fitted Data	A 8
	A.7. Using squared Voltage instead of Kinetic Energies	A 8
	A.8. Effect of Data Misalignment	A 10
	A.9. Ethylene Glycol VS results	A 11
	A.10.Plume Compounds	A 12
В.	Utilized Software	В 13
C.	Acknowledgments	C 14
D.	Selbstständigkeitserklärung	D 15

List of Figures

1.1.	Knowledge Gap between atmospheric models and observations 5
1.2.	Capability of different Reagent Ions
3.1.	VOCUS schematic
3.2.	Ion Source schematic
3.3.	Ion Source and VOCUS Inlets
3.4.	LTOF schematic
3.5.	Multi-Channel-Plate schematic
3.6.	Corroded Ion Source
3.7.	Optimization of Primary Reagent Ion Clusters
3.8.	Distribution of different Ionization Pathways
4.1.	Conventional Calibration Operation Procedure
4.2.	Voltage Scanning Example Curves
4.3.	Correlation of ΔE_{kin}^{50} to Sensitivities
4.4.	Declustering higher Order Nopinone Cluster into lower Order
	Cluster
4.5.	Impact of Voltage Scanning at high Speeds
5.1.	AEROMMA Flight over Chicago 42
5.2.	${ m VS}$ results for ${ m C_2H_6O_2\cdot NH_4}^+$ during the AEROMMA Chicago
	Flight
5.3.	Examples of Ambient Voltage Scans during AEROMMA 45
5.4.	Quantification of oxygenated Compounds in urban Plumes 50
A.1.	Written Instrument Parameters during VS
A.2.	Comparison between $\Delta \mathbf{U}^2_{50}$ and $\Delta \mathbf{E}^{50}_{kin}$
A.3.	Shifting of the calculated $\Delta \mathbf{E}_{kin}^{50}$ values due to misalignment of
	data

1. Introduction

1.1. Air Quality and Climate Change

The Earth's atmosphere consists of gaseous molecules that are kept around the solid landmasses and liquid oceans of the planet by the gravitational forces of the Earth itself. This mixture is mostly comprised of molecular nitrogen (78 % N_2) and oxygen (21 % O_2) as well as Argon (1 % Ar). Besides these compounds, there are varying amounts of water vapor (up to 3 % H_2O) present, depending on the location. Roughly the last 1 % of the atmosphere is made up of so-called trace gases. These trace gases exhibit lower atmospheric abundance in comparison to the previously mentioned constituents. Still, they can have a substantial impact on the local and global atmospheric system, contributing to notable air quality impacts and influencing climate change. [1].

The industrialization of the past two centuries, coupled with an immense increase in the usage of fossil energy sources, has drastically increased the impact humanity has on the global climate by increasing the contribution of trace gases to the atmosphere. The rapid increase of greenhouse gases, which contribute to warming effects, and the increase in volatile organic compounds (VOCs) bring changes in the climate, already evident globally [2]. VOCs act as precursors to aerosol and cloud formation, resulting in cooling effects. The rate at which these climate changes occur is highly likely to surpass the human capacity for rapid and effective adaptation, potentially leading to economic, social, and existential challenges for millions of individuals. However, significant uncertainties currently exist, particularly in the connection between emissions and the chemical evolution of VOCs that can impact cloud formation and, consequently, the planet's energy budget through sunlight reflection.

Parallel to industrialization, the growing human population has led to a rising number of individuals residing in urbanized environments [3]. In polluted areas, air quality significantly impacts the well-being and health of inhabitants [4]. A major health risk arises from high levels of ozone $(\mathbf{O}_3)[5]$ and aerosol particles, specifically

particulate matter smaller than $2.5 \,\mu\text{m}$ ($PM_{2.5}$)[6]. Studies have shown that breathing air with high ozone concentrations can harm the human cardiovascular system, leading to inflammation, and cellular and DNA damage [7]. It is noteworthy that ozone is secondary in nature, i.e., formed via atmospheric chemical reactions of emitted trace gases, and as such, its levels are dependent on the quantities of VOCs and nitrogen oxides [8]. Moreover, $PM_{2.5}$ are one of the largest human health hazards globally. They contribute to health impacts due to the incapability of the human respiratory system to filter them out of the inhaled air. As a result, they can accumulate in the lungs, leading to inflammation [9]. Urban aerosols can be directly emitted by anthropogenic sources as primary organic aerosols (POA). However, recent studies show that a significant fraction of urban aerosol is secondary, with secondary organic aerosol (SOA) being a driving health impacts in urban air [10] [11] [12].

Understanding SOA and ozone formation requires investigating the ever-changing and complex composition, chemical reaction pathways, sources, sinks, and interactions of these pollutants and more importantly their organic trace gas precursors and their oxidation products in urban air. These oxygenated volatile organic compounds (OVOCs) are only partially emitted directly, and formed to a large degree by oxidation of VOCs in the atmosphere. Studying these regional systems is essential not only for enhancing air quality, but also for connecting with the broader context of the global climate and the previously stated issues associated with climate change.

1.2. Changing Emissions of our Complex Environment

In urban areas, such as cities and metropolitan regions, human-caused emissions heavily impact the total emission budget [10]. For a long time, the primary sources of emissions have been mostly combustion engines [13] related to traffic and industrial activities.

To reduce emissions from combustion processes, several effective measures have been put in place over the past few decades [14]. Improvements in catalysts and overall engine efficiency have reduced the pollution from conventional combustion engines [15]. Policies designed to reduce emissions from these sources have not only resulted in the enhancement of combustion engines but have also triggered the use of alternative, environmentally friendly energy sources, including de-fossilized fleets. These policies have led to an overall decrease in the impact of pollution caused by traffic, and are expected to diminish emissions derived from combustion further in the

future. While such mitigation strategies are implemented across numerous regions globally, it's important to note that the improvements are not universal, and there exist substantial variations in the scale of improvement among different countries, cities, and urban areas.

Combustion sources primarily emit constituents such as CO₂, water, and a diverse variety of VOCs [16] as well as NO and NO₂. VOC emissions are not exclusive to combustion processes, but are also emitted by multiple other anthropogenic (e.g., [17]) as well as biogenic sources [18]. Recent studies show that the reduction of combustion emissions has led to the emergence of other pollution sources such as volatile chemical products [19], cooking [20], and construction activity emissions e.g., asphalt [21]. VOC emissions from volatile chemical products include household chemicals that consumers use in their everyday lives, such as cleaning agents, hygiene and cosmetic products, paints, insecticides, and pesticides. Recent novel findings indicate that volatile chemical products have emerged as the largest source of petrochemical organic emissions prevailing over traffic in densely populated cities in the US. In a pilot study performed in New York City during a heatwave, it was shown for the first time that volatile chemical products account for over half of the anthropogenic organic emissions [22],[23] and enhance the formation of ground-level ozone [24].

Volatile chemical products and other urban gas-phase organic emissions can undergo diverse chemical reactions to form lower-volatility products that either condense into existing particles or form new particles, contributing to the SOA mass. However, the contribution of volatile chemical products to SOA pollution is unknown. As shown in Figure 1.1, a long-standing open question has been why chemical transport models underpredict urban SOA when compared to field observations [25–38], with the majority of models highly simplifying SOA formation and pointing towards a missing source that can contribute to SOA pollution. A major reason for the underestimation of urban SOA could be missing anthropogenic sources of VOCs in the inventories of the models that could have a high SOA potential. Such missing VOC precursors could be attributed to understudied emission sources from cooking, asphalt emissions, and more importantly from chemical consumer products [19].

To tackle the challenge of finding and quantifying these emission sources and their air quality impacts, large-scale monitoring of emissions as well as targeted measurements in, around, and above urban areas are necessary. A variety of flexible, field-deplorable scientific instruments is needed, to obtain reliable data on concentrations of gas and particle phase compounds, covering a wide range of compound classes,

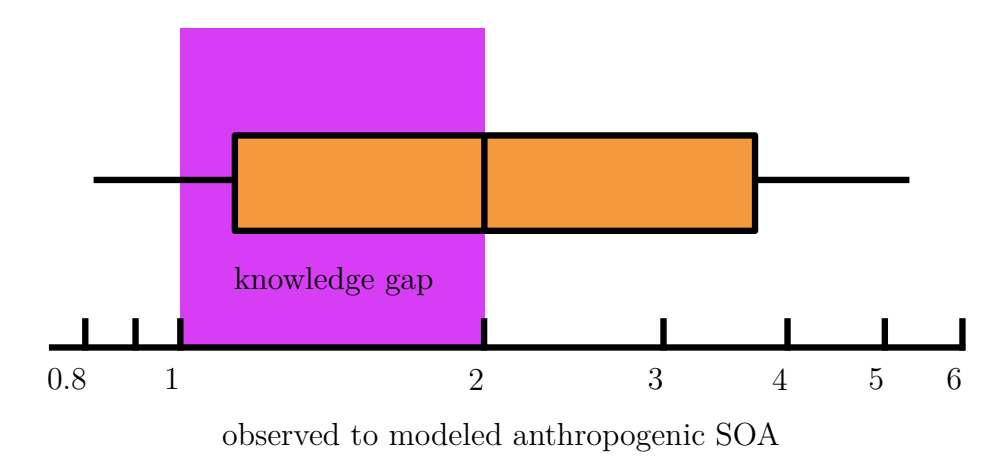


Figure 1.1.: Knowledge Gap between atmospheric models and observations: Ratio of the observed to modeled anthropogenic secondary organic aerosols, as reported in [25–38]. The Box plot shows the discrepancies reported in the studies and the purple area marks the average knowledge gap.

while still being able to measure with high time resolution and specificity to fully understand emission sources as well as VOC and aerosol dynamics and chemistry. While instrumentation to quantitatively measure VOCs that originate from combustion such as aromatics has been successful, the quantification of oxygenated VOCs, OVOCs, with complex functionality expected from volatile chemical product emissions is still in its early stages.

1.3. Instrumentation used for Emission Measurement

To capture a comprehensive picture of the atmospheric composition and the underlying chemical processes, it is essential to conduct measurements encompassing a wide range of compounds of different functionalities and corresponding volatilities. To comprehend the formation of SOA, it is necessary to not only detect but also quantify the potential gas-phase organic and inorganic precursor compounds as well as their oxidation products. Therefore, it is imperative to measure compounds with varying masses, functional groups, and oxidation states.

Each instrumental technique utilizes different properties of the observed compounds to collect information on their chemical and physical characteristics. While spectroscopic instruments observe the characteristic physical interaction of an aerosol or molecule with electromagnetic radiation [39], mass spectrometry techniques utilize the chemical properties of the molecules. In mass spectrometers, sampled molecules

are ionized, and subsequently separated and measured by their mass-to-charge ratio. The mass-to-charge ratio $\frac{m}{z}$ is the compound's mass m divided by the electrical charge gained during ionization, often referred to as z or q. $\frac{m}{z}$ can be referred to as $\frac{u}{e}$ using the units of the unified atomic mass (u) to the elementary charge $e=1.6\times10^{-19}\,\mathrm{C}$. Since the instrument used in this study dominantly charges molecules with only one positive charge, the charge q is assumed to be just e [C], and consequently $\frac{m}{z}$ will be expressed in atomic mass units, u, for ease of reading.

Mass spectrometers are a powerful tool for the analysis of ambient air with both high temporal and mass resolution [40]. Various ionization methods are used to ionize the molecules present in the sampled air. Subsequently, these ionized molecules are subjected to mass separation within a mass-to-charge ratio discriminator and quantified by a detector system. In general, most mass spectrometers do not provide insights on the molecular structure, and thus signals of isomers are indistinguishable [41].

There are different ionization methods used in mass spectrometry and can be classified into two categories: hard and soft ionization methods. Hard ionization methods typically cause fragmentation of the sampled molecules, while soft ionization methods conserve the structural integrity of the molecules. Electron impact ionization is an example of a hard ionization method in which high-energy electrons collide with the analyte molecules, which are the target molecules in the sampled gas [42]. The collision leads to the breaking of chemical bonds in the analyte, resulting in the formation of ionized fragments. Different compounds have different fragmentation patterns, and the information regarding these patterns, obtained through calibration measurements, can be used to determine the original parent molecules. The strength of this method lies in the possibility to measure an extensive mass range; however, the primary challenge resides in the complex analysis and identification of parent molecules, which remains its most significant limitation.

Soft ionization methods predominantly preserve the structural integrity of the observed molecules. A common soft ionization method is chemical ionization mass spectrometry [43]. In this approach, reagent ions are generated in an ion source. These ions themselves are not the focus of the measurements, but rather serve as a means to ionize the analyte molecules. When these reagent ions are mixed with the sampled molecules within a reaction chamber, they react with the analytes resulting in the formation of clusters. These clusters bear the charge of the reagent ion and the combined mass of both the analyte and the reagent ion.

After ionization, a mass discriminator separates the ions spatially by their mass-to-charge-ratio. Various types of mass discriminators are used, some of which utilize magnetic fields to separate the ions [44]. In such sector field mass discriminators, an electric field is applied to accelerate the ions and then the accelerated ions travel through a perpendicular magnetic field. The magnetic field \mathbf{B} acting on the moving ion with the velocity \mathbf{v} and charge q results in a Lorentz force \mathbf{F}_L on the ion, altering its trajectory. Since this force and thus the strength of the acceleration a is dependent on the mass m of the ion, ions of different masses will be spatially separated.

$$\mathbf{F}_{L} = q\left(\mathbf{E} + \mathbf{v} \times \mathbf{B}\right) = m \cdot a \tag{1.1}$$

An array of detectors can then count the ions hitting individual detectors, and with proper calibrations, these counts are assigned to certain mass-to-charge ratios.

Time-of-Flight-mass-spectrometers (TOF) use an electric field to accelerate the ions [45]. They are accelerated as the electric field energy $\mathbf{E_{elec}}$ is converted into kinetic energy $\mathbf{E_{kin}}$.

$$E_{elec} = E_{kin}$$
 (1.2)

$$q\mathbf{U} = \frac{1}{2}m \cdot v^2 \tag{1.3}$$

Ions with higher mass m are moving at a slower speed v within the electric field governed by the applied voltage U. As these heavy ions increasingly lag behind, the longer the path they travel gets. This achieves the spatial separation of ions parallel to their trajectory, allowing a detector to count the ions at the end of the flight path. The time it takes an ion to cover the distance to the detector can be correlated to its mass-to-charge ratio, provided the detector is accurately calibrated. Reduction of collisions between ions and their interactions with remaining neutral molecules within the TOF, is achieved by operating the instrument at low pressures.

After mass separation, a suitable detector counts the ions. The detector is designed to generate an electrical signal that is proportional to the ions hitting it. Such an electrical signal can be a change in voltage or current. Subsequently, the signal is recorded and digitized by a computer system for further data analysis.

Mass spectrometers have found extensive application in the field of atmospheric sciences, primarily owing to their exceptional capability to measure VOCs. The scientific need to expand their capabilities to detect a broader range of chemical compounds, even at concentrations as low as single parts per trillion, has driven significant advancements in recent decades.

1.4. Advances in Mass Spectrometry

Over the last twenty years, many advances have elevated mass spectrometers as an essential tool in today's atmospheric sciences. Significant progress has been made in the development of field-deployable mass spectrometers, accompanied by enhancements in their time resolution and measurement speed. Notable advances have been achieved, particularly with chemical ionization mass spectrometers (CIMS) to improve detection coverage and sensitivity.

No single instrument can comprehensively measure all gas compounds present in the sampled air, especially in a field environment, characterized by numerous unknown and uncertain sources as well as complex atmospheric chemistry. The introduction of new reagent ions has expanded the ability to measure volatile compounds across a wide range of volatility and oxygenation levels.

However, as highlighted in Figure 1.2 the use of certain reagent ions in the CIMS instrument restricts measurement to specific compound classes [46]. This is because not all analyte molecules in the sampled air bind to all reagent ions. Each chemical ionization method exhibits varying sensitivity towards different compound classes and may not ionize certain classes altogether. For the analysis of VOCs, one of the most prominent methods is Proton-Transfer-Reactions Mass Spectrometry (PTR MS), where the reagent ion is a hydron (H⁺) [47], transferred to the analyte by a reaction with H₃O⁺. While PTR performs well for VOCs with low oxidation states, it is not sensitive to higher oxygenated molecules that can play a key role in SOA formation. To expand the detection to more oxygenated gas molecules different ionization methods are required. Common examples of ions utilized in CIMS are: NO₃⁻, I⁻, CF₃O⁻, CH₃C(O)O⁻, CH₅ from Methane ionization, F⁻, Cl⁻ and Br⁻ [41]. In recent years, chemical ionization with the ammonium ion NH₄ has been a focus of research and development [48] [49] [50] to detect oxygenated compounds of increased functionality.

Furthermore, recent developments allow fast switching between multiple reagent ions with a single instrument. This innovation offers the distinctive capability to analyze entirely different VOC compound classes and volatilities within minutes.

In addition to broadening the range of detectable compound classes, significant efforts have been directed toward instrument enhancements aimed at improving sensitivities and mass resolution. Advances in the construction of ion molecular reaction chambers (IMR) have led to reductions in wall losses [51] [52].

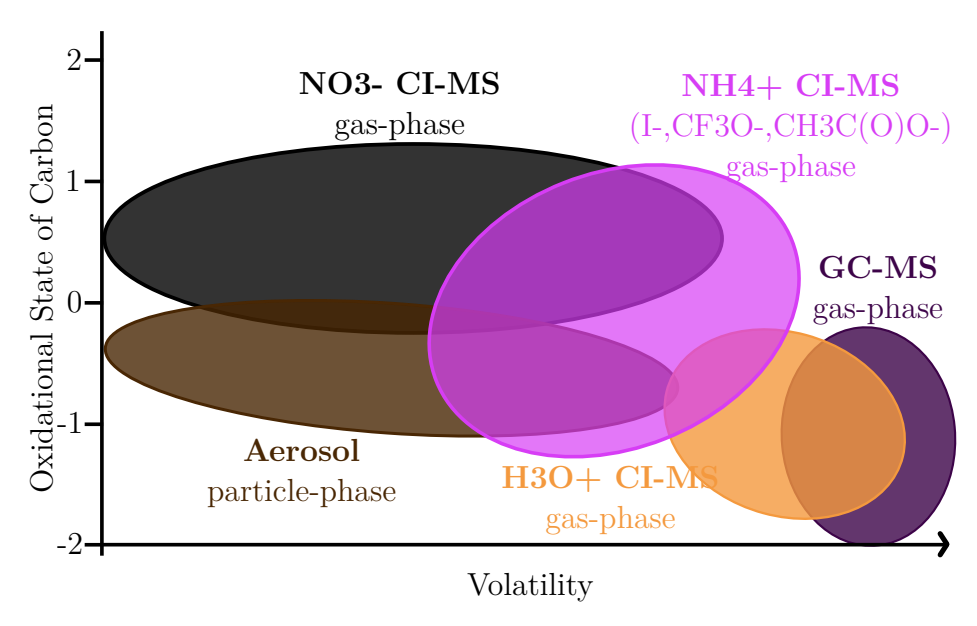


Figure 1.2.: Qualitative representation of the state-of-the-art instrumentation to measure gas-phase components: The volatility range and oxidation state of carbon for compounds detected by each instrument in the gas phase from highly volatile to extremely low volatility organic compounds.

One instrument utilizing the IMR advances, flexible reagent ion switching and possibility to measure with $\mathrm{NH_4^+}$ reagent ions is the VOCUS instrument developed by TOFWERK [53] and Aerodyne Research [54]. With this instrument, it is possible to measure many OVOCs in high mass resolution. The quantification of these measured signals is still challenging and reliable quantification methods are needed. This development is still in early stages and has been primarily tested in laboratory environments.

2. Aims and Objectives

The primary goal of this work is to develop a quantification method for oxygenated volatile organic compounds (OVOCs). Since OVOCs have the potential to form ozone and secondary organic aerosol (SOA) their quantification is highly relevant in urban environments, as both ozone and SOA pose a health risk. Additionally, SOA play a major role in the global climate system and effect global warming processes.

With the VOCUS instrument using NH₄ ionization, measurements of compounds that cover a wide volatility range, including higher mass OVOCs are possible at high time resolution. Due to insufficient calibration methods and standards, the evaluation of measured signals of many of these compounds can only be done qualitatively. In this work, a Voltage-Scanning (VS) technique is developed and optimize, utilizing collision-induced-dissociation processes, to quantify OVOCs, especially those that have not undergone typical calibrations. This includes dependencies of the VS performance on the OVOC concentration levels, as well as the optimization of the methods' time resolution for field applications.

To validate the developed VS technique, field measurements are conducted during the AEROMMA 2023 summer campaign in a collaboration between the Institute IEK-8 of the "Forschungszentrum Jülich" (FZJ) and the "National Oceanic and Atmospheric Administration" (NOAA) team. These measurements are performed under the most challenging conditions aboard the NASA DC-8 research aircraft and allow for the application of the VS method during real-time measurements in a complex field environment. For the first time, the potential of this method in estimating the sensitivity of unforeseen, uncalibrated, and unidentified compounds is investigated in such intricate field environments.

3. Instrument Characterization and Optimization

3.1. VOCUS Principle of Operation

The VOCUS CI-TOF is a chemical ionization (CI) mass spectrometer using a time-of-flight (TOF) mass discriminator [51]. The instrument and related software are manufactured and developed by the TOFWERK AG in Switzerland [53] and Aerodyne in the US [54] and represent a state-of-the-art solution for real-time measurements of VOCs.

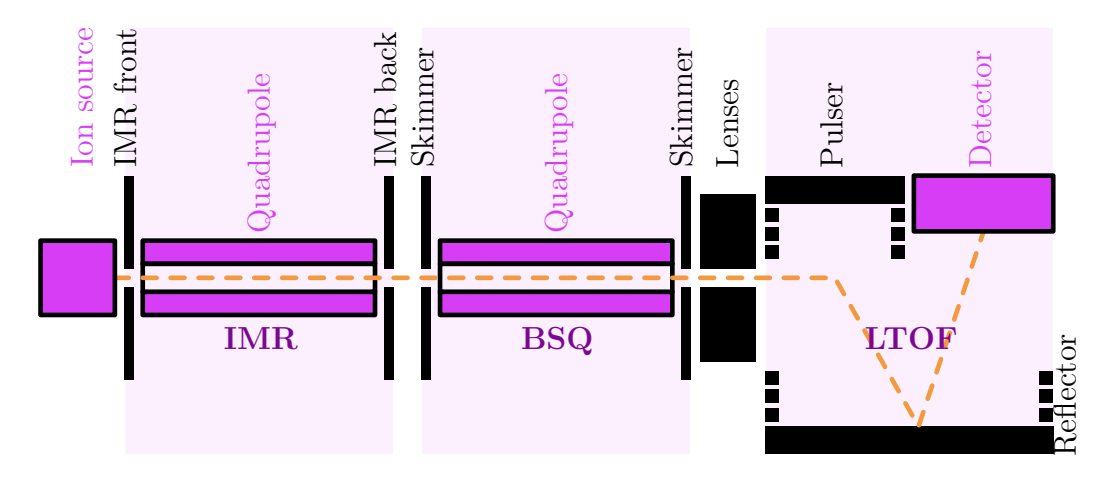


Figure 3.1.: **VOCUS schematic** showing the trajectory of a reagent ion (orange) as it is guided through the ion-molecular-reactor (IMR), where it clusters with an analyte molecule. Subsequently, the ion travels through the big-segmented-quadrupole (BSQ) then proceeds into the long time of flight mass discriminator (LTOF) for mass separation to finally reach the detector.

Figure 3.1 illustrates the operational principle of the VOCUS instrument. Initially, molecules are ionized within the ion-molecular-reactor (IMR) through a reaction with reagent ions produced in the ion source. Subsequently, these charged molecules travel along the ion path through the big-segmented-quadrupole (BSQ) into the long time

of flight mass discriminator (LTOF), eventually reaching the detector.

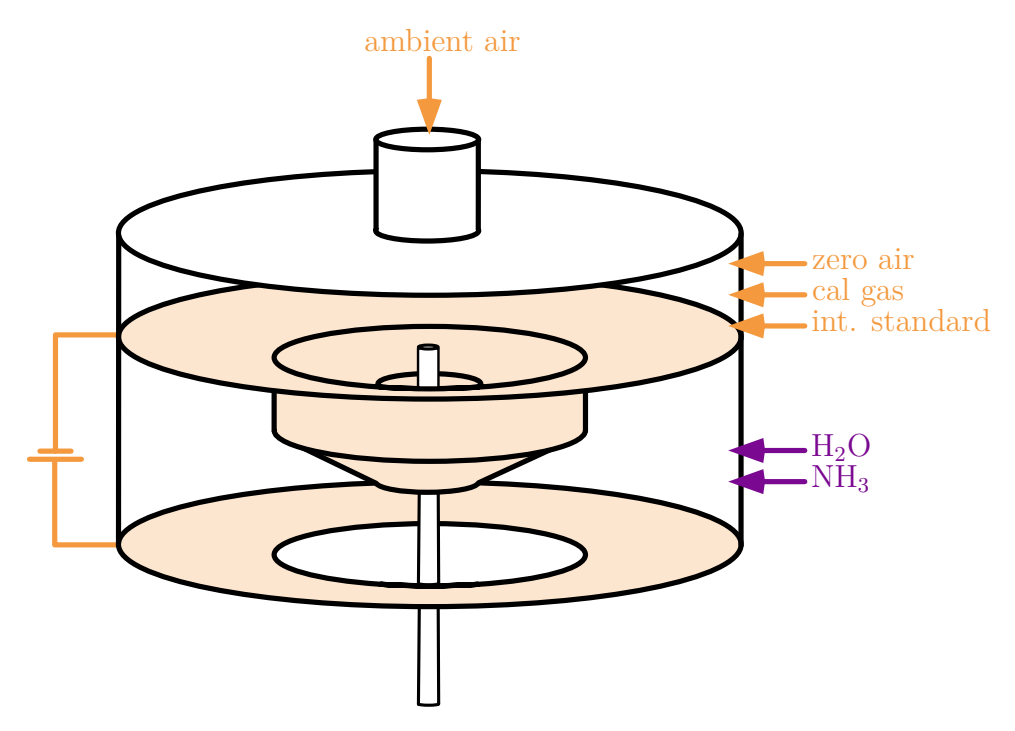


Figure 3.2.: Ion Source schematic. In the upper section, various analytes such as ambient air, calibration gas, internal standards, and zero air can be introduced, mixed. This segment is connected directly to the IMR's inlet via a central capillary. The lower part comprises two electrodes (shaded in light orange) with an applied voltage within the ion source. Reagent ion precursors, namely NH_3 and H_2O , can be introduced to undergo ionization through the discharge plasma of the capacitor. The resulting reagent ions are then channeled towards the IMR, where they combine with the analytes.

In the following, each segment of the VOCUS instrument is described in more detail. Figure 3.2 shows a schematic of the inside of the ion source. The ions for chemical ionization are produced in a low-pressure discharge source consisting of two conical electrodes that generate a discharge plasma when high enough voltages are applied. Reagent ion precursors are introduced into the ion source through inlets on the side as shown in Figure 3.3.

Measurements can be done in different chemical ionization modes with corresponding reagent ions. While measurements in proton-transfer-reaction (PTR) mode are possible, measurements using ammonium ions (\mathbf{NH}_4^+) for ionization have been used in many recent studies to detect more oxygenated molecules and are also used here. To generate ammonium ions, a liquid solution of pure water and a liquid solution consisting of 1% ammonia in water are employed. The equilibrated gas-phase am-

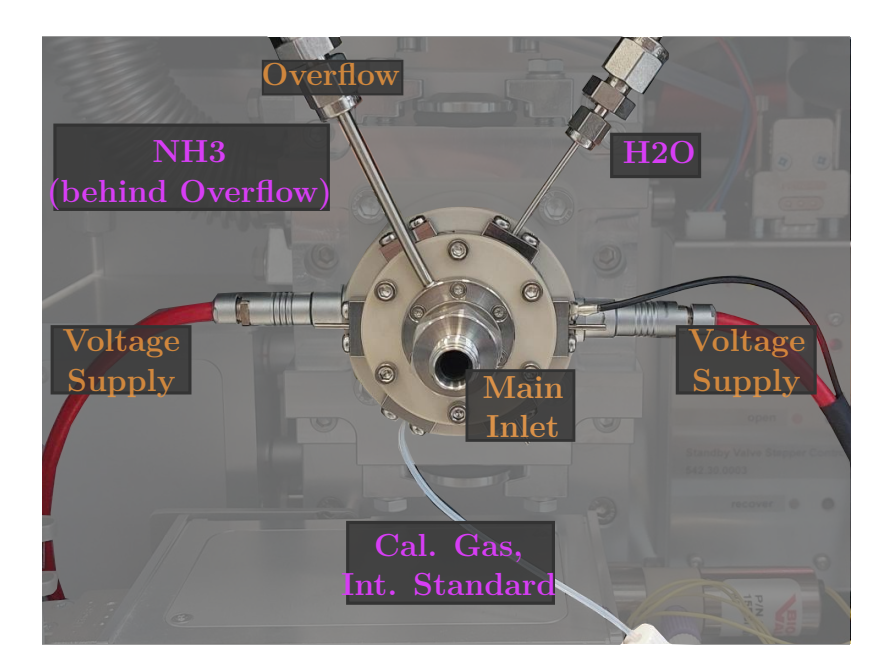


Figure 3.3.: Ion Source Inlets: The front cover of the VOCUS ion source. Through the main inlet, sampled air is introduced. Calibration gas and internal standards are introduced through the bottom inlet and mixed with the sampled air before being pumped into the IMR. The overflow line prevents pressure build-up. The ion source itself is powered by the voltage supplies left and right. NH_3 and H_2O are introduced through the two inlets directly into the ion source, where they mix and become ionized with the NH_3 line directly behind the overflow line.

monia and water over the liquid phase of the solutions are pumped via Teflon lining into the ion source, with flows controlled by two separate mass flow controllers. The gas-phase ammonia and water are introduced into the ion source through a stainless steel capillary, saturating the air inside the ion source. The exact ratio between these two inflows depends on the age of the ammonia solution and environmental conditions, mainly the ambient temperature and the temperature of the transfer lines and reservoirs. In an aged solution, the concentration of ammonium reduces over time and consequently a higher flow is necessary to reach the correct reagent ion distribution in the IMR. For changes in environmental conditions, such as temperatures, ammonium concentrations in the gas phase of the solution can vary. The mixing ratio of water vapor to the 1% ammonia solution is usually around 10:1, but is regulated manually to yield optimal conditions, described in more detail in Section 3.3. To stabilize the system and minimize temperature dependencies, the water reservoir, the water and ammonia lines, and the ion source are heated. The ion source in particular is heated to a constant temperature between 40-50 °C to reduce the condensation of ammo-

nia on the electrodes of the ion source, as shown in Figure 3.6. While heating the ion source reduces condensation, it also introduces more energy into the system that could promote discharge events by increasing the kinetic energy inside the ion source. Temperature optimization is, therefore, necessary to reduce the risk of condensation while limiting any potential discharges. It should be noted that even at optimum temperature conditions, the ion source still shows corrosion signs during measurements, leading to a reduction in performance and potential ion source discharges. The corrosion primarily results from the introduction of ammonia. Therefore, regular cleaning of the ion source is necessary when operated in ammonium mode.

In the ion source, water and ammonia molecules undergo ionization, resulting in the fragmentation of certain water ($\mathbf{H}_2\mathbf{O}$) molecules and the formation of hydronium ($\mathbf{H}_3\mathbf{O}^+$), hydron (\mathbf{H}^+) and ammonium ($\mathbf{N}\mathbf{H}_4^+$) (Equation 3.1). In order for these reactions to occur efficiently, excess water molecules must be present. Furthermore, first-generation ions undergo cluster formation chemistry with water molecules and/or ammonia molecules, as described in Reaction 3.2 and 3.3. Predominantly $\mathbf{H}_2\mathbf{O}\mathbf{N}\mathbf{H}_4^+$, $\mathbf{H}_2\mathbf{O}\mathbf{H}_3\mathbf{O}^+$, and $\mathbf{N}\mathbf{H}_3\mathbf{N}\mathbf{H}_4^+$ clusters are formed. For ideal conditions, the $\mathbf{H}_2\mathbf{O}\mathbf{N}\mathbf{H}_4^+$ cluster should dominate, as it is the cluster required for the ionization chemistry of the analyte molecules. Higher order clusters with more $\mathbf{H}_2\mathbf{O}$ and/or $\mathbf{N}\mathbf{H}_3$ added are also detectable.

$$\mathbf{H}_{3}\mathbf{O}^{+} + \mathbf{N}\mathbf{H}_{3} \longrightarrow \mathbf{N}\mathbf{H}_{4}^{+} + \mathbf{H}_{2}\mathbf{O}$$
 (3.1)

$$\mathbf{NH}_{4}^{+} + n \cdot \mathbf{H}_{2}\mathbf{O} + m \cdot \mathbf{NH}_{3} \longrightarrow \mathbf{NH}_{4}^{+} \cdot (\mathbf{H}_{2}\mathbf{O})_{n} \cdot (\mathbf{NH}_{3})_{m}$$
 (3.2)

$$\mathbf{H}_3\mathbf{O}^+ + n \cdot \mathbf{H}_2\mathbf{O} + m \cdot \mathbf{N}\mathbf{H}_3 \longrightarrow \mathbf{H}_3\mathbf{O}^+ \cdot (\mathbf{H}_2\mathbf{O})_n \cdot (\mathbf{N}\mathbf{H}_3)_m$$
 (3.3)

$$n, m \in \mathbb{N} \tag{3.4}$$

The generated reagent ion clusters are guided into the ion-molecular-reactor (IMR) by a pressure and voltage gradient. In the IMR the reagent ions are mixed with the sampled analyte molecules. These analytes can be either introduced through the big central inlet at the front of the VOCUS instrument, which is used for ambient measurements, or can be introduced through one of the 3 analyte inlets at the side of the IMR (see Figure 3.3). A VOC gas standard is connected to one of these ports for calibrations. Internal standards can be introduced through the second port, introduced at a constant flow of low concentration throughout all measurements to facilitate mass calibrations of the mass spectrum.

The ions travel through the IMR that consists of a drift region in between a quadrupole setup. An applied alternating current on the quadrupole guides and focuses the ions inside the quadrupole. Here the ionization chemistry takes place. The preferred reaction is a ligand switching reaction between the ammonium water cluster $\mathbf{H_2ONH_4^+}$ and an analyte molecule \mathbf{A} . If the affinity for the ammonium cluster of the analyte is higher than the affinity the water molecule has, the ligand, here the ammonium, can switch over to the analyte molecule.

$$\mathbf{H}_2\mathbf{ONH}_4^+ + \mathbf{A} \longrightarrow \mathbf{ANH}_4^+ + \mathbf{H}_2\mathbf{O}$$
 (3.5)

Compared to the direct reaction with an ammonium ion, the ligand switching is a much softer ionization and reduces the risk of fragmentation of the analyte. This occurs because the energy generated by the ligand switching is only equivalent to the difference in binding energy between the analyte ammonium cluster and the water ammonium cluster. After traveling through the IMR region, the newly formed clusters pass the electrode at the back of the IMR and are guided further into the instrument by another voltage gradient. They pass the IMR back electrode and another skimmer electrode to enter the big-segmented-quadrupole (BSQ) region of the instrument. BSQ and IMR have separate pumping paths, and thus the BSQ should mainly contain ionized molecules. This second quadrupole segment further focuses the molecules before they pass a set of lenses to reach the long-time-of-flight mass discriminator (LTOF). The BSQ primarily filters out low-mass ions to minimize the number of reagent ions that do not react with analyte molecules and reach the detector, thus reducing stress on and protecting the detector.

A TOF separates the clusters by mass due to their mass dependent inertia in the applied electric field as shown in Figure 3.4. Heavier clusters reach lower speeds and hit the detector later. Additionally, the TOF of the VOCUS instrument is built as a long-time-of-flight mass discriminator (LTOF). A pulser of the LTOF accelerates the clusters towards a reflector. The pulser generates an electric field for a short time, repelling the charged molecules. They travel through the LTOF and fly into a counter field generated by a reflector. This segment is positively charged and reflects the ions again. Ions with higher impulses make it deeper into this reflector. The impulse they carry is primarily defined by the mass of the compound, but secondarily by the speed that the molecule had at the beginning of the LTOF parallel to the electric field. With the reflection field, the dependency on these speeds and thus the initial kinetic energy of the ions can be eliminated, narrowing broadening effects for measured signals of

ions with the same mass. This enhances the resolution of the system further. After the ions are decelerated, they accelerate again away from the reflector toward the anode, where the detector is located.

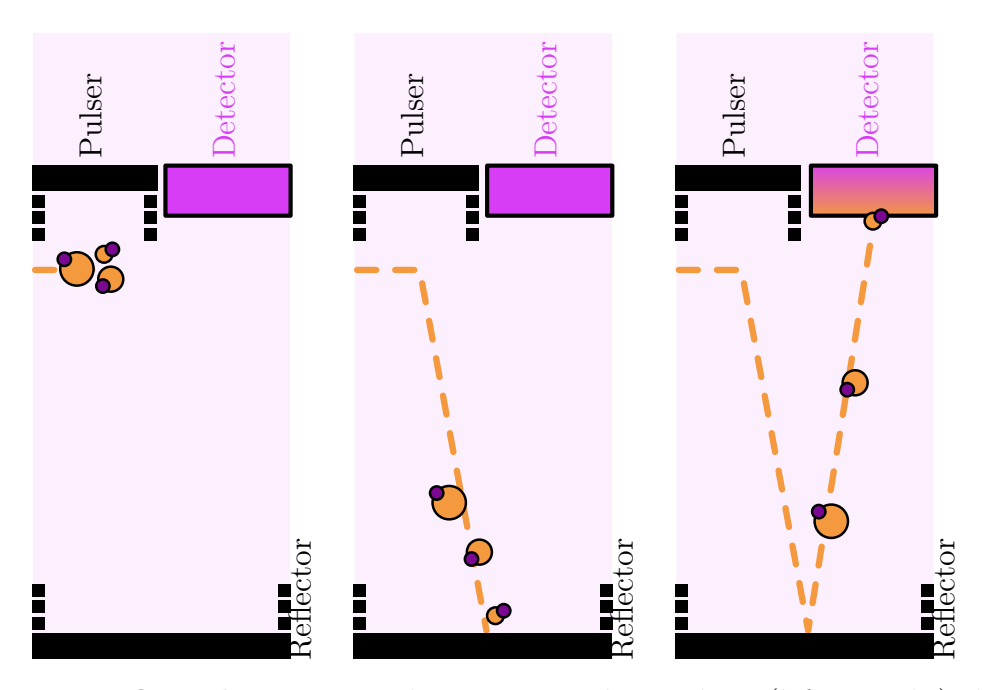


Figure 3.4.: LTOF schematice: Three sequential snapshots (left to right) showing the trajectory of three analytes with distinct sizes (orange) charged by a reagent ion (dark purple). The clusters are accelerated towards the reflector and subsequently directed toward the detector. Throughout their travel, they are spatially separated by mass and are ultimately detected at different times by impacting the detector.

Once the ions have passed the LTOF of the instrument, they hit the detector, which is made up of two multichannel plates (MCP) as shown in Figure 3.5. These plates are stainless steel electrodes with multiple tubes (channels) drilled through them. Each of these tubes functions as an electron multiplier. When the ion impacts the wall of a channel, electrons are knocked out of the wall. Since a voltage is applied to the plate and the electron multiplier channel, the emitted electrons become increasingly accelerated down the channel. The repeated impact of electrons against the channel walls releases additional electrons, leading to the emission of an electron cascade at the opposite end of the channel. For each impacting ion on the upper side of the MCP, several orders of magnitude greater numbers of charge carriers are emitted, thus amplifying the signal to an extent where its detection becomes possible. For further amplification, a second plate is mounted behind the first plate. The electron cascade produced by the first plate subsequently strikes the second plate, initiating

a second cycle of cascades. The final cascade hits an electron collector, that converts the impacts into an electrical signal. Several extractions are performed per second

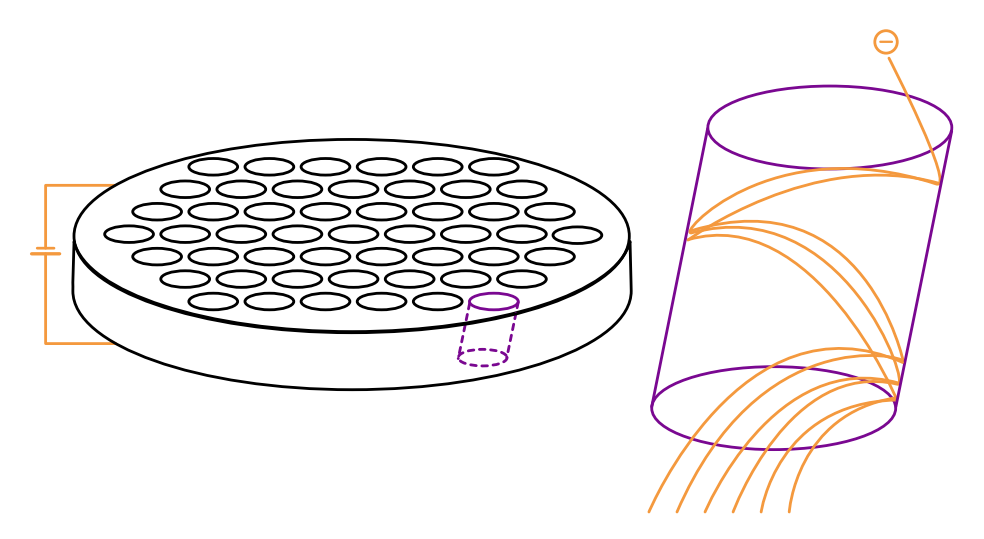


Figure 3.5.: Multi-Channel-Plate schematic: The MCP is a metal plate on which a voltage is applied. In the plate are numerous drillings, functioning as electron multipliers. An exemplary representation of an electron multiplier (purple) is shown on the right. An electron hitting the wall of the multiplier knocks out several additional electrons, resulting in an electron cascade.

and then averaged to obtain a data point. Acquisition times of up to 10 Hz are used in this work. Per acquisition several extractions are performed and averaged. The mass range of measurement are set from 0 to 500 u, while the lower end is predominantly cut off by the quadrupoles, yielding reliable data starting at a mass-to-charge-ratio of around 30-40 u. The measured electrical signal is digitized and processed through the Acquility and TofDaq software from TOFWERK [53]. For mass calibration, peak fitting, and baseline corrections, the TOFWARE software by TOFWERK [53] is used. The time series of the measured, peak fitted, and integrated signals are processed further by Python scripting written as part of this work.

3.2. Minimizing Discharges in the Ion Source

A major challenge encountered during the operation of the VOCUS instrument is the discharging of the ion source. Such discharges would trigger an instrument interlock, halting the ion source current, thereby stopping the analyte ionization, and consequently the VOCUS measurements. In addition, frequent discharging can further increase the accumulation of residue on the ion source electrodes, requiring cleaning.



Figure 3.6.: Corroded Ion Source: Inside part of the front electrode of the ion source after dismounting it. The corrosion, observed when operated with \mathbf{NH}_4^+ ions, is visible. The three inner holes on the right, inside the source, are the inlets of the reagent ion precursor molecules.

Cleaning the ion source takes 2–3 hours, depending on the degree of corrosion, and involves returning the vacuum to ambient pressure, which may result in an increased instrument background once it is reassembled. To measure continuously for days or weeks during a field campaign, the ion source must remain operational throughout the campaign. Therefore, it is crucial to find a solution that can mitigate these restrictions. Additionally, reassembling the ion source may potentially result in leaks, requiring meticulous testing and resulting in even more instrument downtime.

Troubleshooting, performed as part of this work, revealed a noticeable correlation between the discharge frequency and the variable ammonia flow. Additionally, ambient temperature played a role in influencing the discharge frequency, with cooler air leading to more frequent discharges. To mitigate the risk of corrosion and discharges, a heating system is implemented for the ion source and the front section of the IMR. A heating band is affixed around the exterior of the ion source and is insulated with mats and aluminum foil. To maintain stable conditions throughout the operating time and prolong the lifetime of the ion source, a constant temperature of at least 40° C, up to 50° C, is maintained for several hours before operation. This substantially

extended the duration before the ion source showed noticeable signs of discharging, and the VOCUS instrument could be operated continuously in ammonia mode for several weeks before any corrosion signs negatively affected the performance.

3.3. Optimization of the Primary Reagent Ions Distribution

Enhancing the primary ion distribution is crucial for improving the VOCUS instrument's sensitivity to the molecules specified for detection. High counts of the desired reagent ion cluster relative to low counts of all other competing ion clusters have to be achieved in measurements. Following the IMR reactions in Equation 3.1, 3.2 and 3.3, reagent ions can be $H_2OH_3O^+$, $H_2ONH_4^+$, and $NH_3NH_4^+$, as well as higher cluster ions. To ensure that the reaction pathway in Equation 3.5 is prevailing, the dominant ion should be the $H_2ONH_4^+$ cluster. The peak of the $H_2ONH_4^+$ cluster is located at a mass-to-charge-ratio of 36.04 u. Two other significant reagent ion clusters are measured. $NH_3NH_4^+$ at mass-to-charge 35.06 u and $H_2OH_3O^+$ at mass-to-charge 37.03 u. If the latter concentrations are high, the mass spectrum of an ambient measurement becomes significantly more complex. This is because the main ionization might not be the ligand switching reaction, ionizing the analyte with only an \mathbf{NH}_{4}^{+} , but ionization by $H^+ H_3O^+$, $NH_3NH_4^+$, and clusters formed by these three ions with additional H_3N and/or H_2O molecules in the cluster. This leads to single compounds in an ambient sample being ionized by many pathways, thus contributing to the increase of multiple mass-to-charge-ratios for one analyte molecule within a mass spectrum. Such unclean chemistry complicates the evaluation of the data and the attribution of compounds to the observed peaks.

In the \mathbf{NH}_4^+ mode, most of the instrument parameters, especially the voltages of all the components, can be optimized by tuning scripts provided by the manufacturer TOFWERK. Other parameters must be regularly optimized to maintain effective ionization schemes and generate signals with low background levels (see Appendix A.1). For measurements in \mathbf{NH}_4^+ mode, the IMR front voltage is chosen to be 450 V or less, with the IMR back being kept at 0 V. The pressure inside the IMR is automatically regulated to a set value. This value is chosen between 250 and 300 Pa. The flows of $\mathbf{H}_2\mathbf{O}$ gas is tuned in the range between 10-25 sccm and the flow from the ammonia solution is kept in the range between 1-3 sccm, highly dependent on the age of the solution.

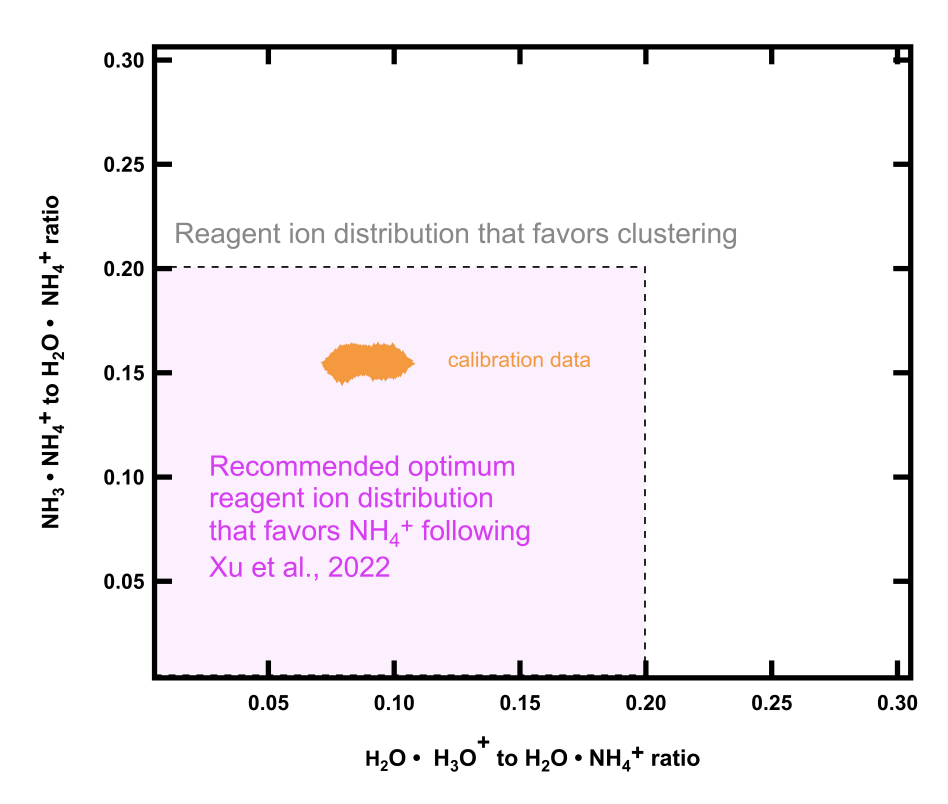


Figure 3.7.: Optimum Regimes of Primary Reagent Ion Distributions: The ratio between the $NH_3NH_4^+$ to $H_2ONH_4^+$ is plotted against the ratio between the $H_2OH_3O^+$ to $H_2ONH_4^+$. The optimal range as recommended by [50] is marked in light purple and is in agreement with the calibration data results from this study (orange).

To optimize the conditions achieved in tuning the flows, IMR pressure and voltages, the work presented by Xu et al. [50] serves as a guide. In Figure 3.7 two ratios between the three main clusters $\mathbf{H}_2\mathbf{O}\mathbf{N}\mathbf{H}_4^+$, $\mathbf{N}\mathbf{H}_3\mathbf{N}\mathbf{H}_4^+$ and $\mathbf{H}_2\mathbf{O}\mathbf{H}_3\mathbf{O}^+$ are plotted against each other. For optimized conditions, the signal of the $\mathbf{H}_2\mathbf{O}\mathbf{N}\mathbf{H}_4^+$ cluster should be at least 5 times larger than the $\mathbf{H}_2\mathbf{O}\mathbf{H}_3\mathbf{O}^+$ and $\mathbf{N}\mathbf{H}_3\mathbf{N}\mathbf{H}_4^+$ cluster signals. After the FZJ VOCUS instrument optimization, the ratios fall within the same range as the signal ratios reported by Lu et al. [50] providing confidence in the primary reagent ions distributions used.

3.4. Ionization Pathways

With the ion source producing various ion clusters, it is crucial to determine the dominant ionization pathways for compounds of different chemical classes. To achieve this, compounds of different functionalities are introduced into the system by injecting

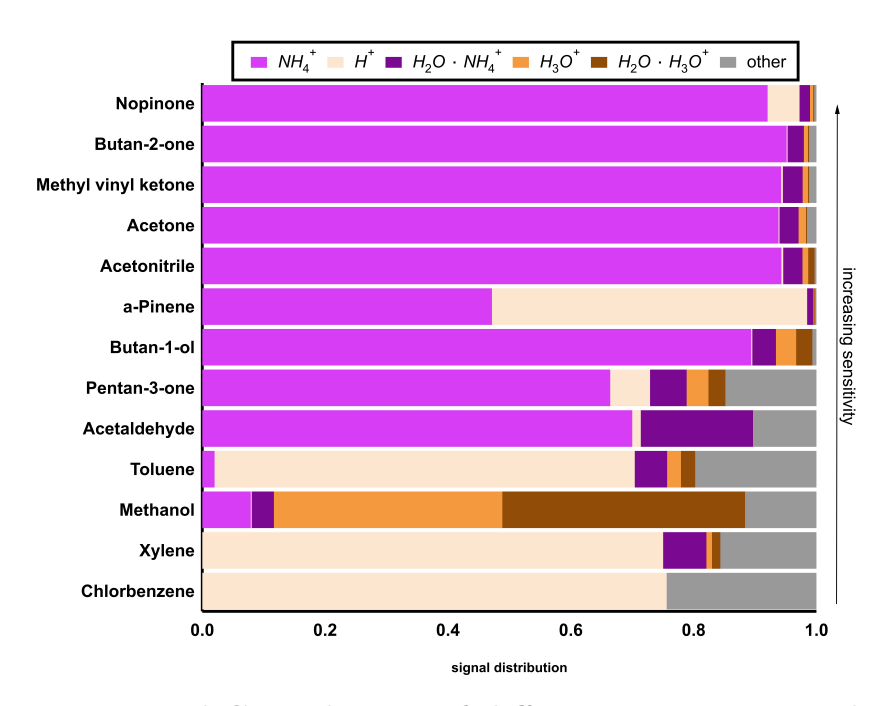


Figure 3.8.: Fractional Contribution of different Ionization Pathways: Fraction of the relative signal to the total signal obtained from various ionization pathways for each analyte ion. The compounds are arranged in increasing order of the VOCUS instrument's sensitivity to the NH_4^+ cluster.

a continuous flow of a calibration gas standard. Details on the gas standards used can be found in Appendix A.3. Ionization occurs as described in Equation 3.6 with A being the compound of interest and R^+ being the reagent ion including ionization by $\mathbf{NH_4^+}$, $\mathbf{H_4^+}$, $\mathbf{H_3O^+}$, $\mathbf{H_2ONH_4^+}$, $\mathbf{H_2OH_3O^+}$, as well as higher water clusters.

$$\mathbf{A} + \mathbf{R}^{+} + n \cdot \mathbf{H}_{2}\mathbf{O} + m \cdot \mathbf{N}\mathbf{H}_{3}$$

$$n + m \le 4$$

$$n, m \in \mathbb{N}$$

$$(3.6)$$

Figure 3.8 summarizes the fraction of each ionization pathway for each compound including ionization by all the above reagent ions.

The ionization is dominated by the \mathbf{NH}_4^+ reagent ion cluster for the ketones, including nopinone, methyl vinyl ketone (MVK), and acetone by over 90 %. High fractional contributions are also achieved for the aldehydes, including butanone, pentanone, and acetaldehyde. Acetonitrile being the only nitrile in the calibration gas standard also shows a dominating \mathbf{NH}_4^+ cluster signal. For alcohols, including butanol and

methanol, a difference is noticeable. While butanol is dominated by the \mathbf{NH}_4^+ ionization, methanol is mainly ionized by $\mathbf{H}_3\mathbf{O}^+$ and $\mathbf{H}_2\mathbf{OH}_3\mathbf{O}^+$. This is because methanol is detected in the lower mass range, where the BSQ cut-off impacts the detection efficiency of compounds, thus highlighting the instrument's limitations rather than ionization inefficiencies. However, compounds that are more challenging to ionize with \mathbf{NH}_4^+ and, therefore, have low sensitivities, exhibit the competing contribution of other reagent ions. This includes α -pinene where a high portion forms a cluster with only the \mathbf{H}^+ ion, as well as the aromatic compounds, namely toluene, xylene, and chlorobenzene, that are primarily ionized through proton transfer reactions.

The method development and optimization presented in this work is carried out using the FZJ VOCUS instrument. However, data collected from the NOAA VOCUS instrument is also included for a later case study. To justify this approach, the instruments are compared in Appendix A.2.

4. Method Development

4.1. Development of Standard Operating Procedure for Calibration and Field Measurements

To accurately assess field data, it is imperative to implement standard operating procedures (SOP) that guarantee the integrity of the data collected and enable efficient processing of raw information. One routine procedure involves adjusting the MCP voltage of the VOCUS instrument, so that the response of ion cluster impacts is aligned with the detector and properly converted into a detected signal that can be processed. This is performed, using software provided by the manufacturer, but is performed in regular intervals to ensure that aging of the MCP is well compensated.

In field measurements, it is necessary to attribute a portion of the measurement time to calibrations and background measurements. During a background measurement, the instrument is solely exposed to zero air consisting of a mixture of nitrogen and oxygen resembling the ratios found in the standard atmosphere. These measures effectively prevent atmospheric air from entering and contaminating the instrument's readings, thus leading to the evaluation of the instrument's pure background. For precise quantification of compounds in ambient air, background measurements are deducted from the data.

In a calibration measurement, the instrument main inlet (see Figure 3.3) is purged with zero air while a controlled flow of gas is introduced through a separate inlet from a cylinder containing known concentrations of a mixture of calibration gases (see Appendix A.3). These gases are relevant VOCs over a wide range of sensitivities. During a calibration, automatic regulation of the calibration flow introduces varying known concentrations to the instrument. Figure 4.1a shows the calibration measurement of acetone following a standard operating procedure. The time series shows the measured acetone signal after final processing including peak fitting of the mass spectra, integration, baseline, and background correction. The calibration steps are the main part of the calibration, marked in Figure 4.1a by the thin purple lines. In the first

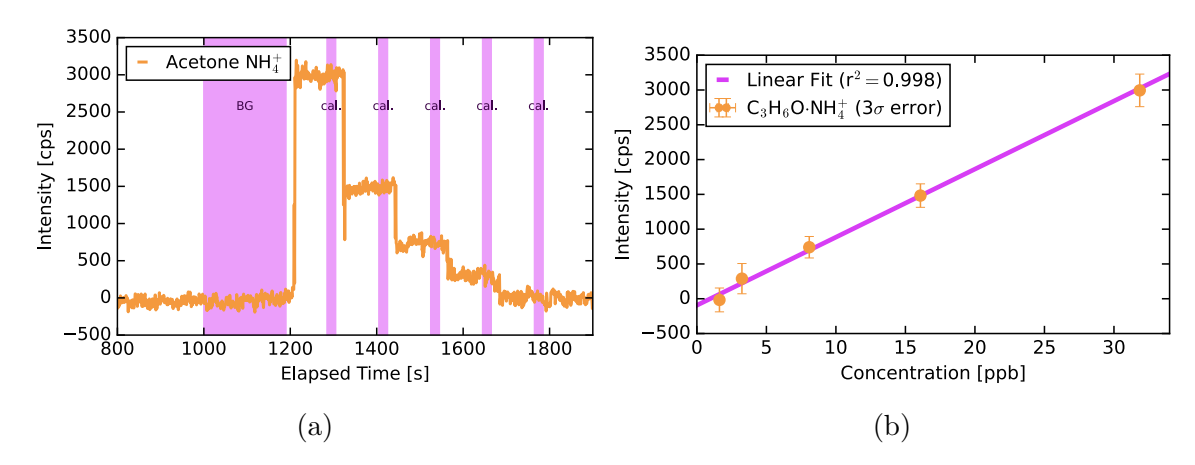


Figure 4.1.: Conventional Calibration Operation Procedure: (a) calibration measurements of acetone at different concentration steps. Marked in dark purple are the calibration averaging periods. The first period is a background period with no calibration gas added. (b) The averaged data of the calibration steps are plotted and fitted with a line. The resulting slope indicates the sensitivity of the instrument for the compound (97.8±2.9 cps/ppb).

step, a high flow is set that corresponds to high concentrations of acetone. After a fixed time, this flow is reduced to lower values and therefore lower concentrations. This is repeated for several steps to obtain the linearity and stability of the calibration and therefore the derived sensitivity. The expected concentrations are then plotted against the averaged signal intensities of the time series measured during the calibration steps. Figure 4.1b shows a linear fit through the averaged data points that yields the sensitivity of the instrument for the calibrated compound. The sensitivity unit is expressed as counts-per-second per parts-per-billion (cps/ppb). The selected time intervals for averaging each calibration step should be of sufficiently lengthy to ensure that the averaged values accurately represent the signal. Furthermore, this averaging should be done for periods when concentrations have stabilized. Arbitrarily short timescales can lead to underestimated concentrations, particularly for sticky compounds with longer equilibration times within the instrument.

The instrument operated in the field and calibrated during this work is the NOAA VOCUS discussed in more detail in Chapter 5. Calibrations of the VOCUS were performed by the Jülich and NOAA teams at regular intervals to ensure the stability of the instrument. More details on the calibrants used during the AEROMMA (Atmospheric Emissions and Reactions Observed from Megacities to Marine Areas) campaign can be found in Appendix A.3. In brief, to reduce data loss and ensure the optimum data quality, calibrations were performed before and after the flights,

and in some cases during transition periods from the airbase to the measurement targets. Overall, the instrument showed reasonable stability through the calibrations over several weeks. Although the instrument was calibrated for a comprehensive list of relevant VOCs, this list was still limited, and not all compounds measured in ambient air were calibrated. Particularly challenging are unknown or unexpected compounds, as well as compounds that pose difficulties for calibration, e.g., sticky functional molecules that are challenging to equilibrate in the instrument lines. This motivates the development of a method to quantify uncalibrated compounds in the field with high precision, and high time resolution even at low ambient concentrations.

4.2. Collision Induced Dissociation to estimate Instrument Sensitivities

To estimate the sensitivities of compounds without doing a conventional calibration, the collision-induced dissociation method can be used, referred to as Voltage Scanning (VS). This method is discussed in detail by Zaytzev et al. [55] and the implementation, and optimization are the primary focus of this work. This method relies on the principle that an instrument's sensitivity to an analyte molecule is proportional to the bond strength between the analyte and the reagent ion. To probe the strength of the cluster bond, the kinetic energy of the cluster is increased continuously until the cluster breaks apart due to collisions with other molecules. In reality, many molecules of the same chemical species, detected at the same exact mass, are measured in a single extraction. The dissociation process of these molecules becomes statistical, and energies are interpreted as energy distributions around a mean energy. Every cluster that is dissociated due to the increased kinetic energy will not be measured by the detector. The decay of the measured signal can be used to get a measure of how strong the analyte reagent ion clusters are bound. An analyte molecule that binds stronger to the reagent ion will result in a lower decline in the signal. To make the comparison of different molecules possible, the value of the kinetic energy at which the signal is reduced by half is used. These kinetic energies at 50% signal strength are denoted as ΔE_{kin}^{50} . Associating ΔE_{kin}^{50} of each compound to the sensitivity obtained from conventional calibrations yields a correlation between ΔE_{kin}^{50} and sensitivity. This correlation can be used to estimate the sensitivity of an uncalibrated compound, by interpreting its ΔE_{kin}^{50} value in the field relative to the ΔE_{kin}^{50} values of known calibrants.

To implement the VS method, the area between the back electrode of the IMR and the front skimmer of the BSQ is selected for adjusting the electric field and, consequently, the kinetic energy of the clusters. As a result, the ionized molecule clusters are increasingly accelerated. The main driver of this dissociation is the collision of the clusters with neutral molecules of the buffer gas inside the drift area. The neutral buffer gas does not experience acceleration within the field, leading to increased collision frequency with clusters as the electric field strength rises. This results in higher kinetic energies for analyte-reagent clusters and, consequently, more vigorous collisions. The field strength is gradually increased by tuning up in parallel the IMR front and IMR back electrode. This maintains the voltage gradient within the IMR, but alters the gradient between the IMR's back electrode and the BSQ skimmer.

4.2.1. Kinetic Energies of Ion Clusters in electrical Field

To provide a more comprehensive physical description and enhance our understanding of the molecular kinetics within the VS region, data regarding the applied electric field and the observed analyte-reagent-ion clusters are translated into an estimated mean kinetic energy value carried by these clusters.

The mean kinetic energy in center of mass frame $\langle \mathbf{E_{kin}^{cm}} \rangle$ (Equation 4.1; [56]) of the cluster formed by the analyte molecule with mass m_a and mean velocity $\langle \mathbf{v_a} \rangle$, and the charged reagent ion, with the mass m_r and mean velocity $\langle \mathbf{v_r} \rangle$.

$$\langle \mathbf{E_{kin}^{cm}} \rangle = \frac{1}{2} \frac{m_a m_r}{m_a + m_r} \left(\langle \mathbf{v_a} \rangle^2 + \langle \mathbf{v_r} \rangle^2 \right)$$
 (4.1)

While the neutral analyte molecules carry no charge and are thus not accelerated by the applied electric field, their mean kinetic energy $\langle \mathbf{E_{kin}^a} \rangle$ (Equation 4.2) is only composed by the thermal energy in the three translational degrees of freedom, neglecting rotations, vibrations, and other excitations, described by the Boltzmann constant k_B and temperature T inside the scanning region.

$$\langle \mathbf{E}_{\mathbf{kin}}^{\mathbf{a}} \rangle = \frac{1}{2} m_a \langle \mathbf{v}_{\mathbf{a}} \rangle^2 = \frac{3}{2} k_B T \tag{4.2}$$

In contrast, the kinetic energy $\langle \mathbf{E_{kin}^r} \rangle$ (Equation 4.3; [57]) of the primary reagent ion $\mathbf{NH_4^+}$, which is assumed to carry a charge of e in C (e = elementary charge) consists of the thermal energy (the same way as for the analyte molecules), the kinetic energy generated by the electric field, contributing as $\frac{1}{2}m_r\mathbf{v_{r_d}}^2$ with the drift velocity $\mathbf{v_{r_d}}$

and the collision kinetic energy, resulting from collisions with the neutral buffer gas molecules that has been estimated to be $\frac{1}{2}m_b\mathbf{v_{r_d}}^2$ while m_b is the mass of the buffer gas [57]. For the analyte molecules, no relative velocity to the buffer gas is assumed and consequently collisions with the buffer gas are neglected.

$$\langle \mathbf{E_{kin}^r} \rangle = \frac{1}{2} m_a \langle \mathbf{v_a} \rangle^2 = \frac{1}{2} m_r \mathbf{v_{r_d}}^2 + \frac{1}{2} m_b \mathbf{v_{r_d}}^2 + \frac{3}{2} k_B T$$
 (4.3)

Using the first part of Equation 4.2 and Equation 4.3, Equation 4.1 can be written as Equation 4.4 and thus as well as Equation 4.5 when using the knowledge about the respective kinetic energies stated in the second part of Equation 4.2 and Equation 4.3. Equation 4.5 can be further reduced to Equation 4.6.

$$\langle \mathbf{E_{kin}^{cm}} \rangle = \langle \mathbf{E_{kin}^{r}} \rangle \frac{m_a}{m_a + m_r} + \langle \mathbf{E_{kin}^{a}} \rangle \frac{m_r}{m_a + m_r}$$

$$\tag{4.4}$$

$$\langle \mathbf{E_{kin}^{cm}} \rangle = \left(\frac{1}{2}m_r \mathbf{v_{r_d}}^2 + \frac{1}{2}m_b \mathbf{v_{r_d}}^2 + \frac{3}{2}k_B T\right) \frac{m_a}{m_a + m_r} + \frac{3}{2}k_B T \frac{m_r}{m_a + m_r}$$
(4.5)

$$\langle \mathbf{E_{kin}^{cm}} \rangle = \frac{m_a}{m_a + m_r} \left(\frac{1}{2} \mathbf{v_{r_d}}^2 (m_r + m_b) \right) + \frac{3}{2} k_B T$$
 (4.6)

With $\mathbf{v}_{r_d} = Z \cdot \mathbf{E}$ [55] and the electric field, $\mathbf{E} = \frac{\mathbf{U}}{d}$ Equation 4.7 is derived. With \mathbf{U} being the applied voltage difference in the scanning region and d the length of the scanning region, which is the region between the electrodes.

$$\langle \mathbf{E_{kin}^{cm}} \rangle = \frac{m_a}{m_a + m_r} \left(\frac{1}{2} \left(Z \frac{\mathbf{U}}{d} \right)^2 \left(m_r + m_b \right) \right) + \frac{3}{2} k_B T \tag{4.7}$$

For the ion mobility, Z Equation 4.8 [55] is used with p and T being the pressure and temperature inside the scanning region, while Z_0 is the reduced ion mobility. The ion mobility describes the ability of a charged particle to move through a medium.

$$Z = Z_0 \frac{101300 \, Pa}{p} \frac{T}{273 \, K} \tag{4.8}$$

The reduced ion mobility Z_0 is given by Equation 4.9 [58] where a, b, and c are empirically derived constants by Steiner et al. [58].

$$Z_0 = a (m_r + m_a)^b + c (4.9)$$

While the conversion method introduced by Zaytsev et al. [55] has gained widespread

acceptance in the scientific community, it is important to acknowledge that a minor error occurred in the derivation due to a citation mistake that was found in this work. Equation 4.7 differs from the original formula by Zaytsev et al.[55] only in the prefactor $\frac{m_a}{m_a+m_r}$, which is used as $\frac{m_b}{m_b+m_r}$, citing incorrectly results by McFarland et al. [56], where the center of mass kinetic energy is derived as presented here. While this error affects only a prefactor and its impact is rather small, it keeps the factor at a constant value, while physically it should scale with the mass of the analyte ion m_a resulting in slightly different kinetic energies for higher mass compounds.

In addition, it should be noted that determining the ion mobility Z accurately can be challenging, especially when taking into account that the reduced ion mobility factor Z_0 is empirically derived by Steiner et al. [58] by combining 10 data points from this study together with several studies by Larriba et al. [59], Ku & Fernandez de la Mora [60], Kilpatrick [61]. Although the agreement of the fit for higher masses (1000 u) is rather good, it is much less accurate for masses below 100 u, characterized by increased fluctuations and a limited number of data points. For many studies of VOCs, the range of masses of interest commonly lies below 400 u. Since the fit parameters a, b, and c are stated without errors and the fit is validated by only a few data points at the lower mass range, the precision of the conversion formula has to be taken cautiously. This is even further amplified by the fact that the ion mobility Z scales quadratic in the conversion shown in Equation 4.7.

A Gaussian error propagation is presented in Appendix A.4. With the error values for a, b, and c unknown, a proper error estimation is challenging. Consequently, error propagation is not chosen to be the indicator of evaluating fitted data in the coming sections.

4.2.2. Implementation and Scripting

VS is performed using the instrument software Acquility [53] for measurements in Germany and a custom LabVIEW program during the AEROMMA mission in the US. The VS is set up by choosing a voltage scanning range, defined as ΔU_{total} (Volts) that depends on the chosen voltage step size ΔU_{step} (Volts/step), the voltage step frequency f (steps/seconds) and the total time t of the whole scan (seconds).

$$\Delta U_{total} = \Delta U_{step} \cdot f \cdot t \tag{4.10}$$

The VOCUS instrument records both the set value and a readout value of all

applied voltages within the measurement data files. The data structure is designed in a manner that the instrument parameters, such as voltages, are recorded less frequently than the mass specta. This approach enhances writing efficiency and reduces file sizes. Additionally, the values of both the set and readout voltages show delays not matching the observed mass spectra decays (see Appendix A.5). The observed signal decays in the mass spectrum are observed almost instantaneously, whereas the readout values exhibit a delay of several seconds and occasionally show stagnation and jumps. Hence, in this study, we assume that the scripting occurs instantaneously, and the VS voltages are calculated based on the elapsed scanning time rather than the written values. This assumption is essential given that the written values show drastic jumps and lags further discussed in Appendix A.5.

The elapsed time values are converted into voltages, using Equation 4.10 and subsequently converted into changes in kinetic energies as described in Section 4.2.1. The temperature T and pressure p in the region are regularly monitored and assumed to be constant. This further reduces the computational time required to process a VS and the dataset's file size.

4.2.3. Estimation of the Kinetic energy at half decayed Signal

Figure 4.2 shows an exemplary data set of three compounds from a VS performed during a calibration. The signal intensity is background corrected and normalized to the maximum intensity measured during the VS period in the data set of interest. These values are then plotted against the kinetic energies, which are converted as described in Section 4.2.1.

To make the decays of the different data sets comparable, the value ΔE_{kin}^{50} is derived for each data set of interest during a VS. This generates a characteristic parameter for each compound's decay rate relative to its signal at 50%. One method to acquire a value for ΔE_{kin}^{50} is to simply select the data point that is closest to half of the intensity at the specified ΔE_{kin}^{100} , with ΔE_{kin}^{100} being the change in kinetic energy at 100% of the measurement signal at the start of the VS. While this technique is computationally efficient, it is susceptible to errors. In a noisier measurement, the selected data point could potentially be an artifact resulting from the noise. Moreover, the density of data points is relatively low for rapid VS measurements, increasing the probability of biases in the chosen ΔE_{kin}^{100} . Using a fit function to approximate the behavior of the observed decays is a more accurate approach that minimizes the uncertainties. A function is fitted to the dataset, with the initial ΔE_{kin}^{100} corresponding to time zero of

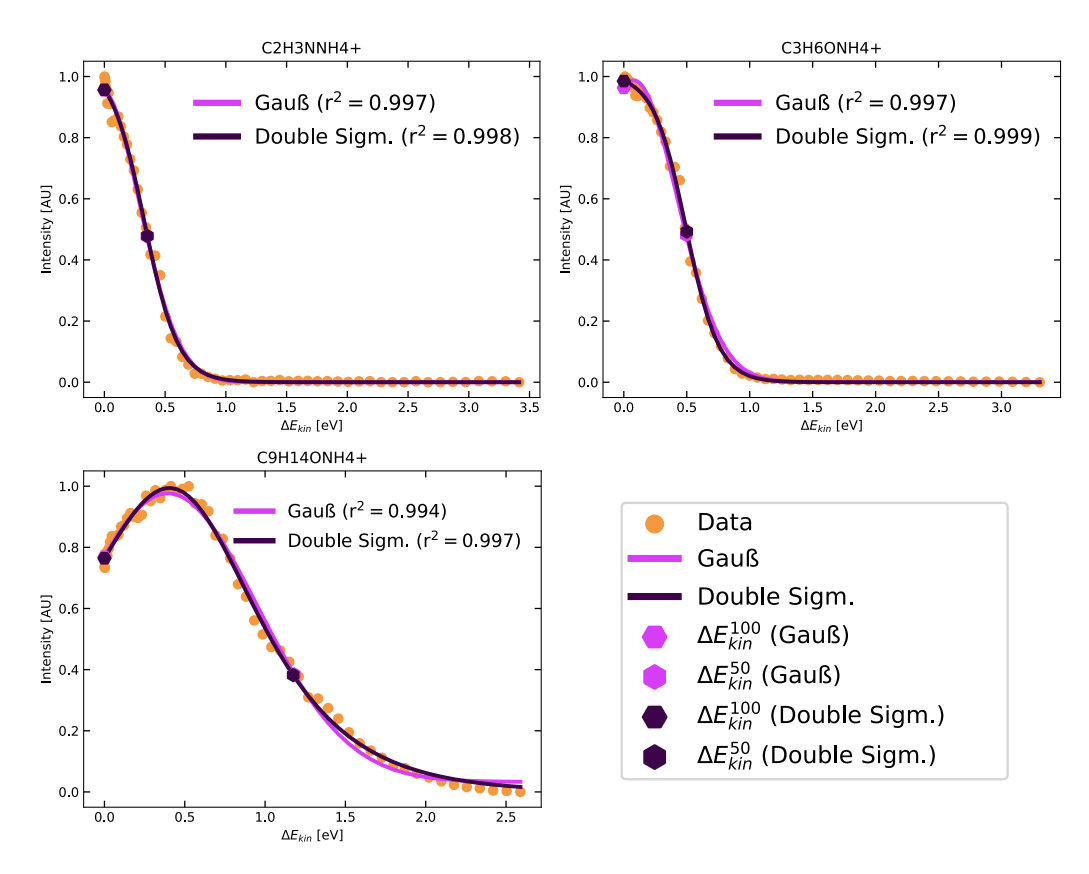


Figure 4.2.: Examples of Voltage Scanning Curves: Three examples of VS curves using different calibration compounds that highlight the range of possible responses to the VS method. The intensity of the data (orange) is normalized to the highest and lowest values of the observed data set. A Gaussian fit and the associated ΔE_{kin}^{50} and ΔE_{kin}^{100} values are displayed in purple. The same approach is followed for a double sigmoidal fit and its results are in dark purple.

the VS where no additional kinetic energy is applied. ΔE_{kin}^{50} is then calculated using the inverted fit function at half of the initial ΔE_{kin}^{100} .

In the examples shown in Figure 4.2, it is apparent that the signal for certain compounds can exhibit an initial increase before subsequently declining. The variation of voltages inside the instrument appears to affect not only declustering, but also other aspects of the instrument's measurement efficiency. This suggests that a stronger electric force may lead to an improved focusing of certain clusters into the BSQ. It is observed that these rising signals generally only appear for higher mass clusters, highlighting potential mass dependencies influencing the VS outcome.

Two distinct functions are proposed and implemented as fitting functions in this study. One function is a Gaussian normal distribution with the Equation 4.11 fitting the observed signal intensities Int as the dependent variable and the independent

variables Int_0 as the base intensity, ΔE_{kin}^c as the center and w as the width of the distribution.

$$Int = Int_0 + A \cdot e^{\left(-\frac{-((\Delta E_{kin} - \Delta E_{kin}^c)^2}{2 \cdot w^2}\right)}$$
(4.11)

This equation performs effectively under various conditions, requiring four parameters Int_0 , A, ΔE_{kin} , and w. This fit is relatively fast and can be effectively applied to a larger number of scans. However, the fit does not ideally describe the physical processes. A more accurate fit, which takes into account physical factors that can influence the VS better, can be achieved using a double sigmoidal fit (Equation 4.12), consisting of a falling and a rising sigmoidal function.

$$Int = Int_{max} \cdot \frac{1}{1 + A \cdot e^{a \cdot \Delta E_{kin}}} \cdot \frac{1}{1 + \frac{B}{e^{b \cdot \Delta E_{kin}}}}$$
(4.12)

The descending sigmoidal function can be interpreted as a representation of collision-induced dissociation, which is the process of interest. On the other hand, the ascending function may indicate potential mass-dependent focusing effects, combined with other factors that could lead to an increase in the signal. The second fit function reaches even better agreement with the data and offers greater flexibility, particularly in VS measurements of compounds characterized by a distinct ascending phase. This function depends on 5 fitting parameters (Int_{max} , A, a, B and b) and requires 5 times more computational time compared to the Gaussian fit. Additionally, the function cannot be analytically inverted, and an extra fitting step must be added to the script for estimating the ΔE_{kin}^{50} value further increasing computational times. In the upcoming sections, the employed fit will always be specified. Regardless of the selected fit, a minimum of 50 data points per VS is chosen to guarantee adequate data fitting conditions.

Although the double sigmoidal fit captures various factors influencing the VS trends, future research is encouraged to unravel and characterize the mechanisms behind the ascending and descending signals observed in the fitting function. While such understanding may aid in mitigating mass-dependent interferences and enhancing VS outcomes, it is not the primary focus of this study.

4.2.4. Correlating Result to calibrated Sensitivities

To quantify VS results and convert ΔE_{kin}^{50} to sensitivities, it is essential to perform VS during conventional calibrations. Compounds selected for calibrations need to cover the entire sensitivity range of the instrument and serve as reference points for evaluating VS results for compounds of unknown sensitivities. A VS measurement with calibration compounds injected into the instrument results in generation of coresponding ΔE_{kin}^{50} values as discussed in Section 4.2.3. Calibration sensitivities, derived

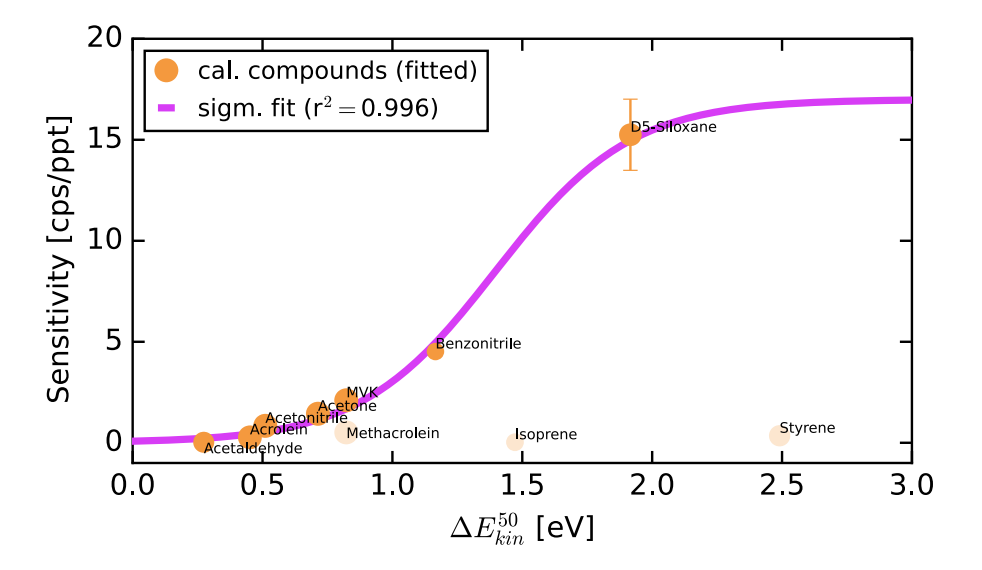


Figure 4.3.: Correlation of ΔE_{kin}^{50} to Sensitivities: Averaged Sensitivities from the NOAA VOCUS instrument (Table A.2) are plotted against the results of a calibration VS during the AEROMMA campaign flight. A sigmoidal fit (purple) is applied to the calibration compounds marked in orange. Methacrolein, Isoprene, and Styrene are not included in the fit but are displayed to highlight possible outliers.

following Section 4.1, are then plotted against the ΔE_{kin}^{50} values. A dependency is described by Equation 4.13 which is fitted to the dataset. The dependent variable sensitivity Sens (Equation 4.13) is described as a function of the independent variables $Sens_{max}$ describing the maximum sensitivity of the instrument, the center of the slope $\Delta E_{kin}^{50center}$, a factor for the width of the slope area $E_{kin}^{50width}$ and an offset for a minimal sensitivity $Sens_{min}$.

$$Sens = Sens_{max} \cdot \frac{1}{1 + e^{\frac{\Delta E_{kin}^{50} - \Delta E_{kin}^{50}eenter}{E_{kin}^{50}width}}} + Sens_{min}$$

$$(4.13)$$

In Figure 4.3 an exemplary data set is shown following calibrations performed before a flight over Chicago during the AEROMMA campaign. Averaged calibration sensitivities are plotted against their ΔE_{kin}^{50} values. A sigmoidal curve is fitted, omitting certain compounds that exhibit significant deviation from the anticipated behavior. Such compounds, including styrene, isoprene, and methacrolein as well as other aromatics, display considerably higher ΔE_{kin}^{50} values than predicted by the fitted curve from their sensitivities. The cause of this variation is linked to classes of compounds that are less responsive to collision-induced dissociation and suffer from low sensitivities, but are also influenced by multi-reagent ion charges, as shown in Figure 3.8. To ensure that ambient concentrations are not overestimated, compounds that strongly deviate from the curve are currently excluded and a higher sensitivity threshold fit is chosen. Such fit could lead to an overestimation of sensitivities and consequently an underestimation of the concentration of certain compound classes in ambient air. Given that such compounds typically exhibit low sensitivities and their signals are weak, an overestimation of their sensitivity would further suppress these signals. On the contrary, if the sensitivity for these compounds was underestimated, the concentrations in the sampled air would be overestimated with possible biases in evaluating their air quality impacts.

In future research, it will be vital to investigate the VS response to diverse compound classes in order to identify which molecules in ambient air may be underestimated when using this method. Such research will contribute to precisely quantifying compounds with a wide range of functionalities. In the current study, our emphasis is on compounds that correspond to the fitted upper sensitivity limits and are responsive to \mathbf{NH}_4^+ chemical ionization.

4.2.5. Error Propagation and Uncertainties of the VS Method

To evaluate the precision, accuracy, and dependability of the VS method, several sources of uncertainty are examined. The conversion of the measured time series into kinetic energies, as outlined in Section 4.2.1, presents various challenges. Errors for the measured instrument parameters, including temperature and pressure, are rather low, due to high stability and constant PID (Proportional-Integral-derivative) controlling. However, the uncertainty of the applied voltages and the assumed ion mobility are found to be the main drivers of error. For the set voltage, the primary sources of uncertainty are the readout and alignment challenges. For the ion mobility, on the other hand, the formula used is based on empirical data derived by Steiner

et al. [58] from a dataset with rather low density in the mass range relevant for this study. Nevertheless, the parameters used in the fit derived by Steiner et al. [58] describe the data in the study relatively well, but the lack of proper documentation of errors makes it challenging to validate their accuracy. Given that both the applied voltage change and the ion mobility scale quadratically into the conversion function, their errors can have a great impact.

In an example calculation for a VS of nopinone, the E_{kin} value corresponding to 80 V is determined using the Gaussian error propagation presented in Appendix A.4. At 80 V, approximately half of the signal has decayed. Assuming a voltage error of ± 5 V, a temperature error of ± 2 K, a pressure error of ± 0.1 Pa, an error of ± 0.5 mm for the length of the scanning region and no error at all for the reduced ion mobility, the calculated value falls to $E_{kin} = 1.5 \pm 0.6(44\%)$ eV that represents a lower limit of the propagated error. However, when introducing uncertainty for the reduced ion mobility, the error of E_{kin} increases rapidly, challenging the validity of employing Gaussian error propagation without a more in-depth examination of Steiner et al.'s fit results. It is worth noting that further simplification of the error propagation of E_{kin} is possible, as discussed in Appendix A.7. Since E_{kin} correlates to the square of the applied voltage change U², fitting the VS signal against U² can not only reduce error propagation uncertainties but more importantly decrease computational time.

In this study, the quality of the fitted VS function data and observed noise levels will be used to assess errors, rather than relying on error propagation during conversions. For the uncertainty of the fits used for the decaying signal of VS measurement, the coefficient of determination (r^2) is used as the primary indicator of the quality of the resulting ΔE_{kin}^{50} value (see Appendix A.6). Fits with an r^2 exceeding 0.98, during for example high-intensity calibration periods, are considered reliable and are frequently observed. However, for compounds with noisier VS results, a poor signal-to-noise ratio in the data set limits the quality of the fit and results in a lower r^2 value. In this study, fits with r^2 lower than 0.3 are excluded from further analysis and only ΔE_{kin}^{50} derived from well-fitted fits are taken into account for further evaluation. To mitigate the possibility of erroneous data interpretation during complex field measurements, multiple VS measurements are conducted to enhance the accuracy and statistical robustness of the observed trends.

4.2.6. Declustering into lower Order Clusters

The signal of a $\mathbf{A} \cdot \mathbf{N} \mathbf{H}_4^+$ cluster, where A is the analyte molecule and $\mathbf{N} \mathbf{H}_4^+$ is the ammonium reagent ion, occasionally displays an initial rise at the start of a VS measurement, as demonstrated for nopinone in Figure 4.2. A higher order cluster, such as $\mathbf{A} \cdot \mathbf{H}_2 \mathbf{O} \mathbf{N} \mathbf{H}_4^+$, where an additional water molecule is added to the cluster, is measured at a higher mass to charge ratios in the mass spectrum. As the voltages increase during the VS, the kinetic energies of the molecules rise, and one water molecule can dissociate from the cluster, resulting in the formation of a lower-order cluster of $\mathbf{A} \cdot \mathbf{N} \mathbf{H}_4^+$. This would result in an increase in the signal measured at the mass of the lower order cluster. To investigate, we utilize the calibration compound nopinone as an illustration of a compound with extended rising periods during VS measurement and heightened sensitivity. In Figure 4.4 these measurements are shown as a function of tuned voltage $\Delta \mathbf{U}$ against normalized intensity. When comparing the data set

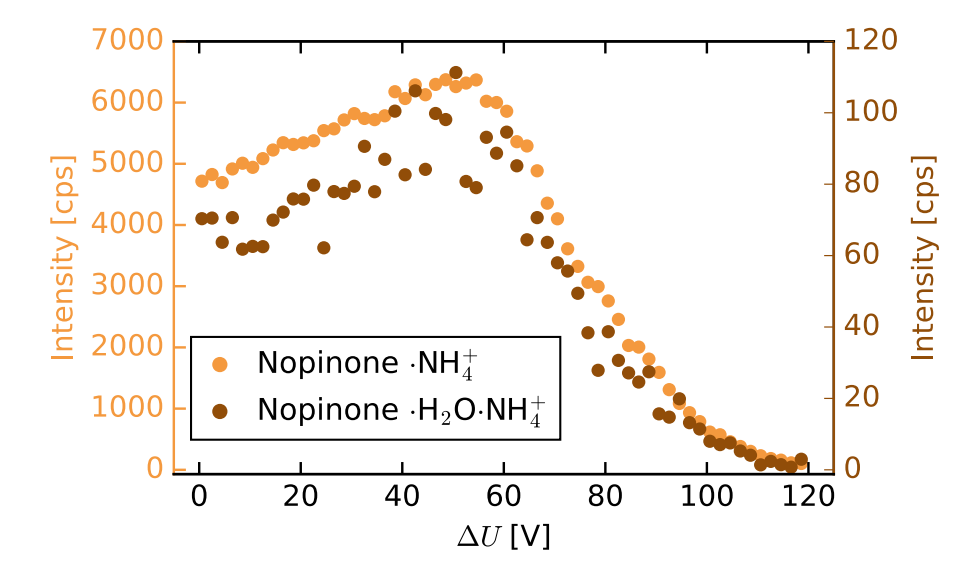


Figure 4.4.: Declustering of higher Order Nopinone Clusters into lower Order Clusters: Intensities of the VS measurement for the different Nopinone clusters highlight the negligible influence of declustering. Voltages have not been converted into kinetic energies to highlight the response.

of the Nopinone· \mathbf{NH}_4^+ cluster and the Nopinone· $\mathbf{H}_2\mathbf{ONH}_4^+$ cluster, a nearly identical pattern is observed. The Nopinone· $\mathbf{H}_2\mathbf{ONH}_4^+$ exhibits the same rising trend at the beginning of the VS and starts dropping off around the same ΔU as the Nopinone· \mathbf{NH}_4^+ . Additionally, the Nopinone· $\mathbf{H}_2\mathbf{ONH}_4^+$ signal is 60 times smaller than Nopinone· \mathbf{NH}_4^+ , making it even more unlikely for this mechanism to be of relevance. Other clusters of

even higher order or clusters with added NH_3 molecules are also observed, but only show signal strengths orders of magnitude lower than that of the Nopinone $H_2ONH_4^+$. In conclusion, declustering or fragmentation of other compounds and clusters with higher mass is unlikely to explain this increasing phenomenon.

4.2.7. Voltage Scanning Optimization

To ensure the effectiveness of the VS methodology during field experiments, it is imperative to minimize scanning time while still achieving satisfactory outcomes at different signal intensities. This holds particular significance for the utilization of the VS method in demanding environments, like the rapidly shifting conditions encountered during an aircraft measurement campaign.

A series of measurements is conducted to test and determine optimized VS setup parameters. For these measurements, calibration gas is injected into the instrument at four different flow rates and thus four different concentration levels. In each of these concentration steps, six VS measurements are performed at a 10 Hz step frequency, matching the acquisition frequency of the instrument during aircraft campaigns. To reduce the total scanning time while maintaining a total scanning range of 120 V, the step size is reduced for each of the 6 VS measurements, thus reducing the number of data points collected per VS.

In Figure 4.5 exemplary VS results for the calibration compounds nopinone and acetonitrile are shown. The spread of the measured ΔE_{kin}^{50} values increases notably for faster scanning speed. For nopinone, the spread widens significantly only for scans faster than 1.5s, while for the acetonitrile only the scan of 6s shows reasonable stability across the different measurements. Notably, there is no clear trend observable for the concentration dependency of the VS results. This is expected, as the VS should only provide decay rates of relative magnitude and should not be influenced by the total signal, provided that the signal is strong enough to conduct a proper VS initially. A noticeable rise in the average ΔE_{kin}^{50} for both compounds is observed for faster VS. This can be explained by challenges related to the readout and alignment of the set voltages during the VS that are expected to increase as the total VS time decreases. Given that the sensitivity function in Figure 4.3 will change under different VS conditions and different instrument setups, we highlight the necessity to always optimize the VS method for each instrument in use. Ambient VS measurements should be evaluated, using the exact same conditions to avoid biases related to VS time-dependent variabilities as highlighted in Figure 4.5.

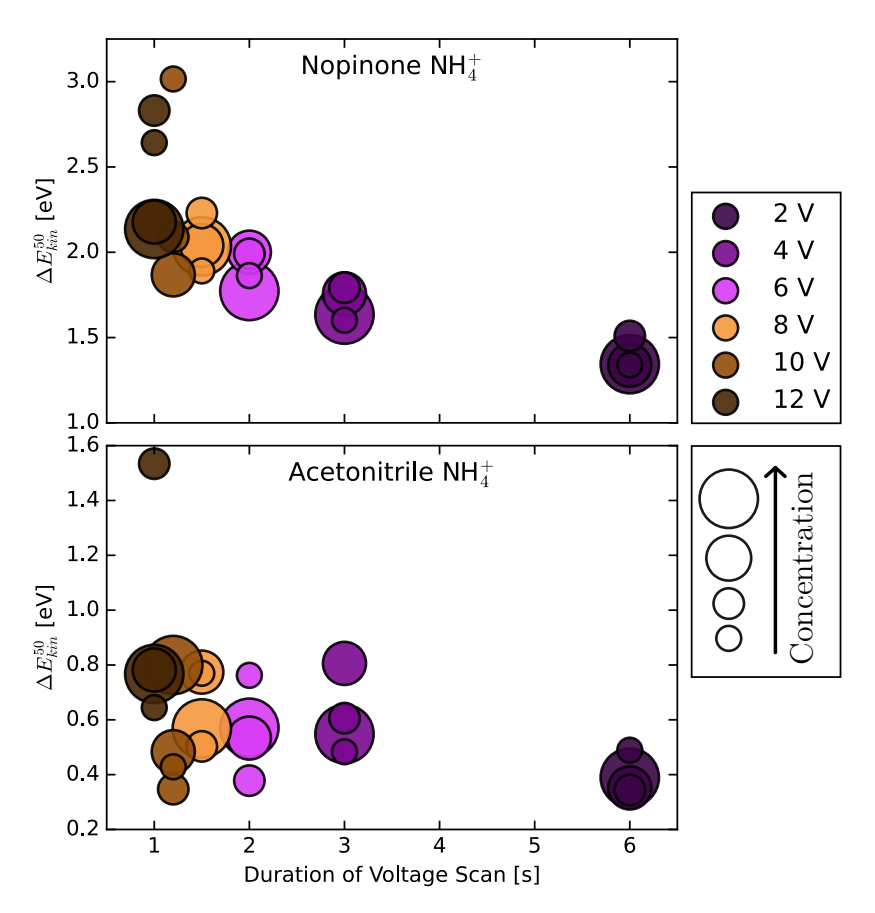


Figure 4.5.: Voltage Scanning Performance at Various Concentrations and Time Resolutions: Results obtained from a series of Voltage Scanning experiments conducted at different speeds and calibration gas flows, with marker size indicating the flow rates. The compounds used for the tests are Nopinone and Acetonitrile, representing high and low sensitivity compounds, respectively. The measurements were carried out with a 10 Hz acquisition and scripting frequency, and the step size for each scripting step is indicated in the legend.

In measurements using only zero air, without the introduction of calibration gas or ambient air, it is apparent that a high instrument background can complicate the interpretation of the resulting ΔE_{kin}^{50} . This is particularly challenging when interpreting ambient measurements at very low concentrations that compete relative to the background signal. To minimize such influences on the VS results, it is important to reduce the instrument's background as much as possible. This can be achieved by optimizing the vacuum system, reducing any leakages, utilizing high-purity gases and solutions, and ensuring precise tuning of the detector (see Appendix A.1).

Overall, the optimization of the VS method carried out in this study reveals for the first time that it can be streamlined to just a few seconds while maintaining its reliability and reproducibility, even at lower concentrations. Consequently, this method can be of great value in field measurements, including complex airborne investigations, allowing for the quantification of oxygenated compounds with unknown sources for the very first time.

Implementation of Voltage Scanning during AEROMMA Campaign

The VS technique has the unique potential to estimate sensitivities of unknown or uncalibrated compounds in a complex field environment. With the objective of this work so far being the testing and optimization of the VS method, the following section will highlight an implementation example of the VS method during the AEROMMA campaign in 2023.

The AEROMMA (Atmospheric Emissions and Reactions Observed from Megacities to Marine Areas) campaign took place in the summer of 2023. For a period of more than two months, the NOAA Chemical Sciences Laboratory team, with the support of international partners including Forschungszentrum Jülich GmbH, conducted measurements using the NASA DC-8 scientific aircraft. During the initial phase of the campaign, the measurements focused on oceanic emissions of sulfur compounds, while in the subsequent phase, urban environments were the primary target. Several instruments capable of measuring particle and gas phase compounds were deployed to probe the plumes from marine areas as well as from various US and Canadian megacities and metropolitan areas, including Los Angeles, New York, Chicago, and Toronto. A major emphasis of the AEROMMA mission is not only to identify and measure VOC emissions and their sources, but also to advance our understanding of the potential for these emissions to contribute to the formation of secondary pollution, including SOA and ozone. In the following, focus will be given on the AEROMMA VS results from the NOAA VOCUS instrument operated by the Chemical Sciences Laboratory team in collaboration with scientists from Jülich.

The VS method is implemented to minimize data loss in ambient measurements while still ensuring high-quality VS results following the optimization results of this study. The total scanning range for a VS is set to 100 V, a scanning frequency of

 $10\,\mathrm{Hz}$ matching the instrument acquisition speed is used, resulting in a total scanning time of $5\,\mathrm{s}$ ($2\,\mathrm{V/step}$). The scans were conducted at regular intervals using automated software scripts, as well as through manual initiation, to ensure the quantification of compounds when the aircraft is flying over urban plumes.

In this work, one of the flights conducted over the Chicago area is selected for exemplary detailed analysis. An example compound is thoroughly discussed, with a particular emphasis on the implementation and performance of the VS technique.

5.1. AEROMMA Flight over the Chicago metropolitan Area

To demonstrate the effectiveness of the VS technique, the flight over the Chicago metropolitan area on August 1st, 2023, starting and ending at the airbase in Dayton, is chosen for further analysis. This flight is selected as an ideal case study since 16 ambient VS measurements were conducted over 9 hours of ambient measurements (starting at 8:45 local time), with a significant fraction occurring during high-intensity urban plumes.

Figure 5.1 shows several maneuvers including upward and downward spirals performed in close proximity and downwind of Chicago as well as over industrial highly polluted areas in the region. Additionally, the time series of the ion cluster at the mass-to-charge-ratio of $\mathbf{C}_2\mathbf{H}_6\mathbf{O}_2\cdot\mathbf{N}\mathbf{H}_4^+$ is presented. This compound is likely ethylene glycol, which is considered of potential urban origin due to its strong correlation with nitrogen oxides (\mathbf{r}^2 =0.8), which are typically emitted from combustion sources. In the $\mathbf{C}_2\mathbf{H}_6\mathbf{O}_2\cdot\mathbf{N}\mathbf{H}_4^+$ time series, 10 periods of high signal intensities are observed. These are considered primarily urban plumes of interest, displaying increasing signals for multiple compounds throughout the mass spectrum.

To find and isolate potentially relevant compounds from urban emissions, the averaged mass spectra during these plume periods are calculated. These spectra are then compared to average spectra during a background period marked as BG in dark purple, as shown in Figure 5.1. This background period is not associated with the instrument background; instead, it represents the chemical composition of air outside urban plumes, measured at low altitudes within the boundary layer, characterized by low signal intensities. It should be noted that although there appear to be intervals with less variability and weaker signals, these are simply transit periods when the aircraft is operating at higher altitudes, and thus, not collecting notable information

relevant to the goals of the campaign. By comparing low and high pollution periods, several compounds are isolated that show a significant increase in signal within urban plumes. The $\mathbf{C}_2\mathbf{H}_6\mathbf{O}_2\cdot\mathbf{N}\mathbf{H}_4^+$ time series in Figure 5.1 represents one of the most prominent compounds enhanced in urban plumes.

In the following, the performance and potential limitations of the VS technique for compounds enhanced in urban air will be discussed. Focus is given on $C_2H_6O_2\cdot NH_4^+$ with the highest average urban increase of around 390 cps, attributed to ethylene glycol, a chemical used in antifreeze product, coolants, paints, and inks.

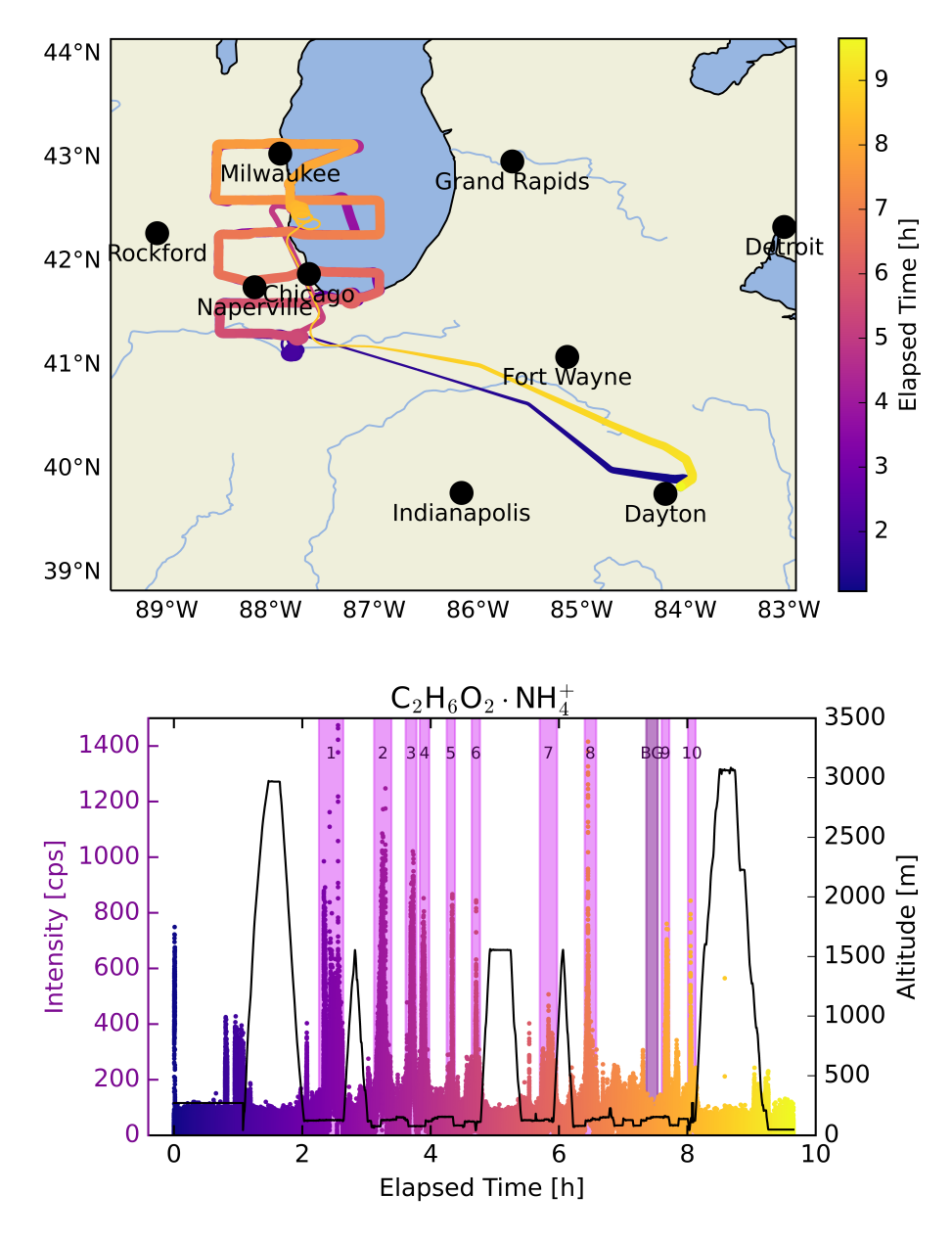


Figure 5.1.: **AEROMMA Flight over Chicago:** In the upper plot, the flight path is shown, where the line width corresponds to flight altitude, with thicker lines representing lower altitudes. In the lower plot, the time series of $C_2H_6O_2 \cdot NH_4^+$ is presented, and it includes identified plume periods marked in purple and one ambient background period highlighted in dark purple. The time elapsed after the start is indicated as 13:44:52 UTC/8:44:52 CDT.

5.2. Quantification of Ethylene Glycol Concentrations using the VS Method

The results of the VS calculations for the $C_2H_6O_2\cdot NH_4^+$ time series are shown in Figure 5.2. The VS data is converted to kinetic energies and a double sigmoidal function is utilized to fit the results as described in Equation 4.12. The VS results during background measurements (dark purple markers 0,1,2,3) as well as during periods of low ethylene glycol signal in ambient sampling (lighter purple markers 1,2,3,5 and 12) exhibit low r^2 values and high variability. This is expected as during these periods, no significant signal is present, and the VS is essentially performed over background noise.

As highlighted in Section 4.2.5 fits with r² lower than 0.3 are excluded from further analysis to estimate sensitivities. When disregarding these VS results, the remaining VSs still exhibit considerable variation. Although the fits are significantly better compared to the background VSs, some distinct outliers persist. A high portion of the data points lies in a range at around 1 eV (4,6,13,14,16,17), while other VSs are spread over a range of higher eV values up to 2.35 eV. To understand the causes of these variations, a detailed investigation of all the time series of the VS measurements is performed.

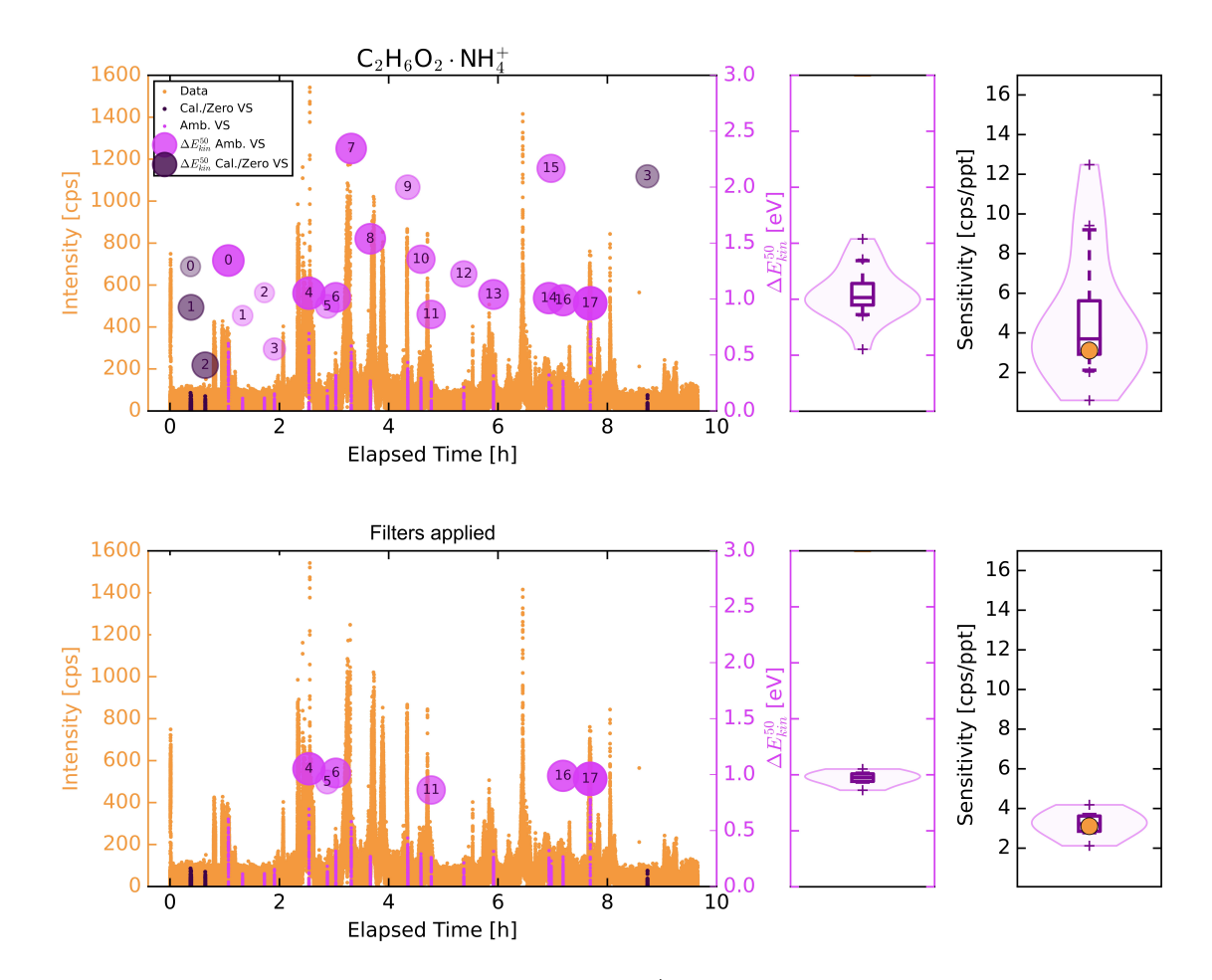


Figure 5.2.: VS results for $C_2H_6O_2\cdot NH_4^+$ during the AEROMMA Chicago Flight: In the left time series, the data points used for the VS fitting are indicated. The $\Delta E^{50}kin$ results for the respective VS data section are displayed on the second y-axis. The size and opacity of the $\Delta E^{50}kin$ markers are adjusted based on the r^2 of the fit, with the number of the VS labeled in circles for easier identification. Darker purple shading is used for periods when the VS was conducted during a background measurement. The Violin plots on the right provide a summary of the $\Delta E^{50}kin$ values for the VS measurements shown in the corresponding left plot. The rightmost plot illustrates the sensitivities corresponding to these $\Delta E^{50}kin$ values together with the measured sensitivity of Ethylene glycol in the lab (orange circle). In all the violin plots, median values for the upper and lower quartiles are presented. The top row shows the spread for all VS results, while the bottom row is limited to only the valid VS results.

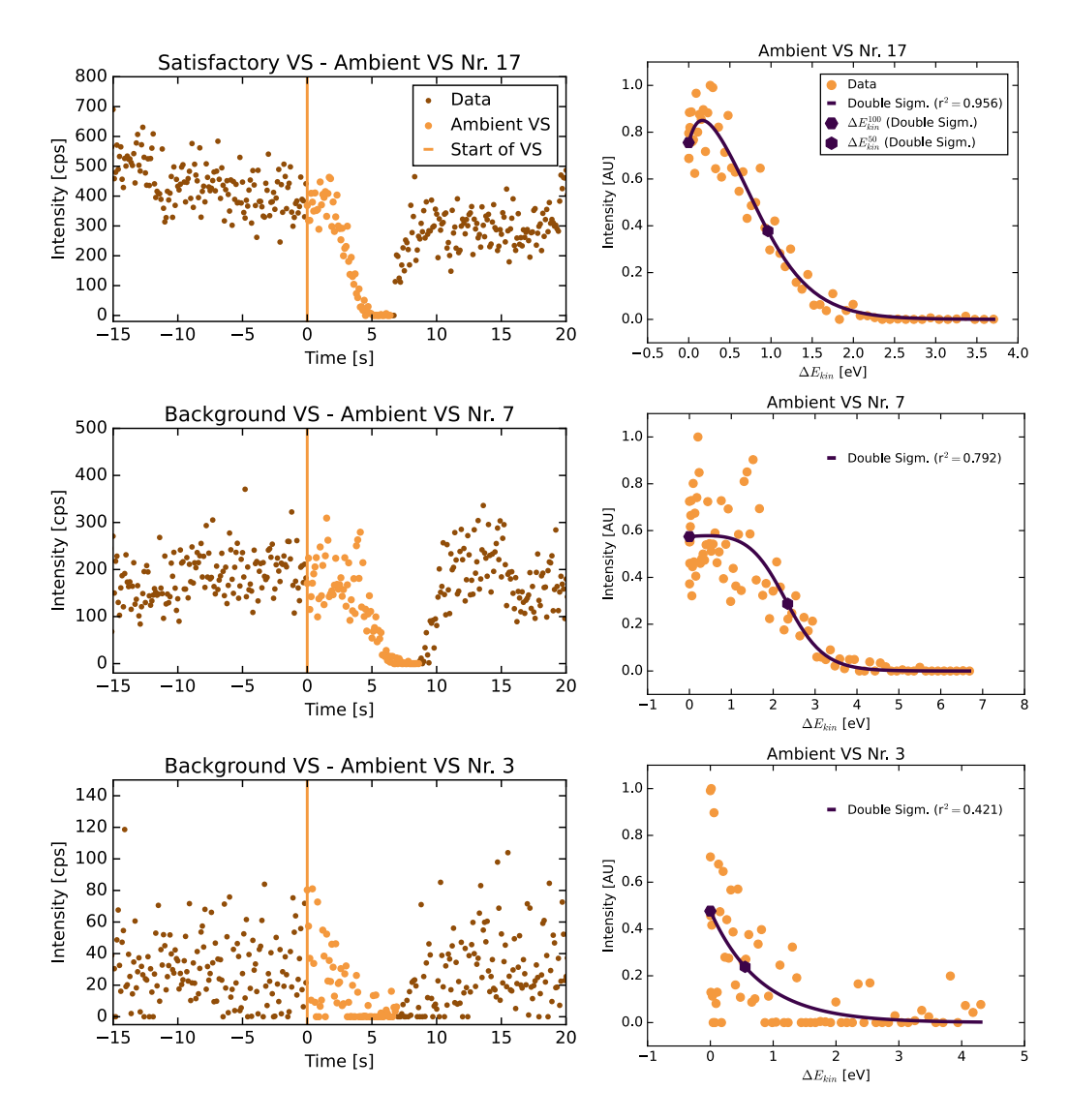


Figure 5.3.: Examples of Ambient Voltage Scans during AEROMMA: VS measurements of the $C_2H_6O_2\cdot NH_4^+$ time series during the first flight over the Chicago metropolitan area. On the left side, the raw data is presented, with the start of the VS period and the data points within the VS period marked in lighter orange. On the right side, the same data is shown after conversion into kinetic energies, with a double sigmoidal fit applied to it. The $\Delta E^{50}kin$ and $\Delta E^{100}kin$ values are indicated in dark purple. The first row represents a best-case scenario with a well-performed VS 17. The second row illustrates VS 7 and highlights observed issues related to the alignment of the voltage steps and mass spectra data acquisition. The third row demonstrates VS 3, characterized by very low signal levels, and serves to illustrate VS uncertainties during a background period.

VS 17 5.3, performed during a high signal period at 200 to 700 cps, shows a curve matching the expected behavior observed during the laboratory optimization experiments. Although the data exhibit significant noise, the descending trend is clearly observed in the raw data. The fit function is in a satisfactory alignment with the data with an r² of 0.96 showing a minor signal increase at the start of the VS. With a total scanning time of 6.4 s, the VS is 1.4 s longer than the intended 5 s highlighting that instrument communication delays impact VS results, even for VS case studies like VS 17, which show good performance. Scanning times between 6 and 7 s are observed in many of the VS measurements (see Appendix A.8). With the scanning times of the reference calibration VS being in the same range, a comparison between these values is feasible.

In VS 7 the ΔE_{kin}^{50} value is at 2.35 eV with an r² of 0.79. The decrease in the fit's accuracy is partially due to the increasing signal-to-noise ratio in the data at lower concentrations, which is approximately two times lower compared to VS 17. However, the overestimation of ΔE_{kin}^{50} is due to the extended scanning period of 8.6 s, which is 3.6 s longer than the set value. The most likely explanation for these discrepancies is lags in the communication between the LabVIEW program used for prompting the scripting and generating commands to change voltages, and the instrument computer, which sets and reads out the instrument parameters, such as voltages. Such instrument communication lags can be challenging since they lead to data misalignment and consequently, a fit that overestimates the ΔE_{kin}^{50} of the VS. Communication lags mentioned here as well as their effects are discussed in more detail in Appendix A.5 and A.8. Due to their substantial potential to affect the accurate determination of sensitivities, this study excludes VS measurements with a total scanning time exceeding 7s and this way the significantly exceeding the calibration scanning time. The scans exceeding the set duration limit are VS $0(7.2 \,\mathrm{s})$, $7(8.6 \,\mathrm{s})$, $8(7.1 \,\mathrm{s})$, $9(16 \,\mathrm{s})$, 10(7.1 s), 12(7.1 s), 13(7.3 s), 14(7.1 s), 15(10 s).

Several options for improving future analyses with respect to this communication lag are proposed. Efforts to optimize the communication between the hardware components and the scripting software are essential. Such changes have been communicated to the instrument company, and collaborative efforts to address these communication lags are currently underway. It is crucial to emphasize that these improvements do not affect the campaign data that have already been collected. For already measured data, one option could be to use a time series of a different compound as a proxy. For example, during the AEROMMA mission, D6-acetone, a deuterated com-

pound not naturally present in ambient air, is used as an internal standard. This compound is continuously introduced into the instrument to facilitate accurate mass calibrations for each flight. During the VS measurements the D6-acetone fit function showed a relatively concise shape. Given its consistent presence during all measurements, the D6-acetone decay curve could be used to normalize the timing of the VS and therefore precisely derive the true set voltages. Such corrections could then be applied to all other time series, resulting in a shift of set voltages to better match their realistic values. However, implementing such a procedure will need extensive and careful coding, testing, and optimization and is planned for the near future. With these optimizations in place, the variability of the VS results is expected to be greatly reduced, resulting in much more stable results.

In the last example shown in Figure 5.3 (VS 3), an ambient scan at very low ethylene glycol concentrations is shown. VS 3 is performed during a high altitude transit period from Dayton to Chicago that shows low signals over the majority of the mass spectrum. It is evident that the rapid signal drop can be interpreted as background suppression. The fit yields a ΔE_{kin}^{50} value that is much lower than the results from the other VSs but has a low \mathbf{r}^2 value of around 0.42. Given that the average signal in the ambient measurements before and after the VS is presumably almost zero, the result from the VS fitting should reflect noise and should be excluded from further analysis. To avoid the contribution of background fits to the estimated sensitivities, fits with intensities within the variability of the instrument background are excluded.

Another potential source of uncertainty, not currently emphasized in the case studies shown in Figure 5.3, could arise when the VS is conducted during periods with rapidly increasing or decreasing signals. Such rapid concentration gradients during a VS could compete with the decays imposed by the VS and therefore bias the fit function high or low. While this effect is worth investigating further in the future, for the data presented in this work data alignment limitations overshadow possible other effects by far.

The valid ambient VS results of $C_2H_6O_2\cdot NH_4^+$ are shown in Figure 5.2 (more details in Appendix A.9). Although more than half of the VS are currently excluded due to the above limitations, the remaining VS provide consistent results with reduced variability in the ΔE_{kin}^{50} calculation. The remaining ΔE_{kin}^{50} of VS 4, 5, 6, 11, 16, and 17 are used to calculate an average $\Delta \bar{E}_{kin}^{50} = 0.97 \pm 0.07 (7.2\%)$ eV. After conversion into sensitivities, using the fitting parameters for the sigmoidal slope described in

Section 4.2.4, a sensitivity of 3207±723(23%) cps/ppb is estimated.

Conventional calibrations of ethylene glycol were performed after the AEROMMA campaign by Chelsea Stockwell of the NOAA team. The derived sensitivity is found to be 3110±119(3.8%) cps/ppb, when calibrating the NOAA VOCUS instrument in lab conditions. This result is in great agreement with the 3207±723(23%) cps/ppb derived with the VS method. Such findings therefore further promote the use of this method for estimating sensitivities for uncalibrated compounds, as well as for compounds with unidentified sources that may be challenging or impossible to calibrate.

5.3. Quantification of Key oxygenated Compounds in urban Plumes

In the following, the method is tested for a number of additional compounds, that are relevant in urban plumes. Compounds with the 13 highest urban enhancements are used to estimate sensitivities based on their VS results following the same approach as for the ethylene glycol time series. Only fits of VS with less than 7s and r² values higher than 0.3 are considered. However, it should be noted that the current analysis of these compounds is not evaluated and optimized in the same depth as it is for the ethylene glycol resulting in larger variability.

VS sensitivities are compared to the sensitivities of compounds that were calibrated during the campaign. The displayed calibration results from conventional calibrations are in decent agreement for most compounds. While D5-siloxane, and acetone give similar results and agree within 9 and 3%, benzaldehyde has a noticeable discrepancy. Being a low-sensitivity compound towards ionization by ammonium clusters, benzaldehyde sensitivity is overestimated by the VS method and follows a similar pattern as isoprene and styrene previously discussed in Figure 4.13. It should be noted that, for the majority of these compounds, comparing the calibration results to the VS results is inherently circular, as these calibration results were originally used to convert ΔE_{kin}^{50} values into sensitivities. Agreement between these datasets should therefore be expected. However, the fact that ethylene glycol was calibrated after the campaign and was not considered for the conversion fit makes the strong agreement between the ethylene glycol calibration and the VS result particularly promising.

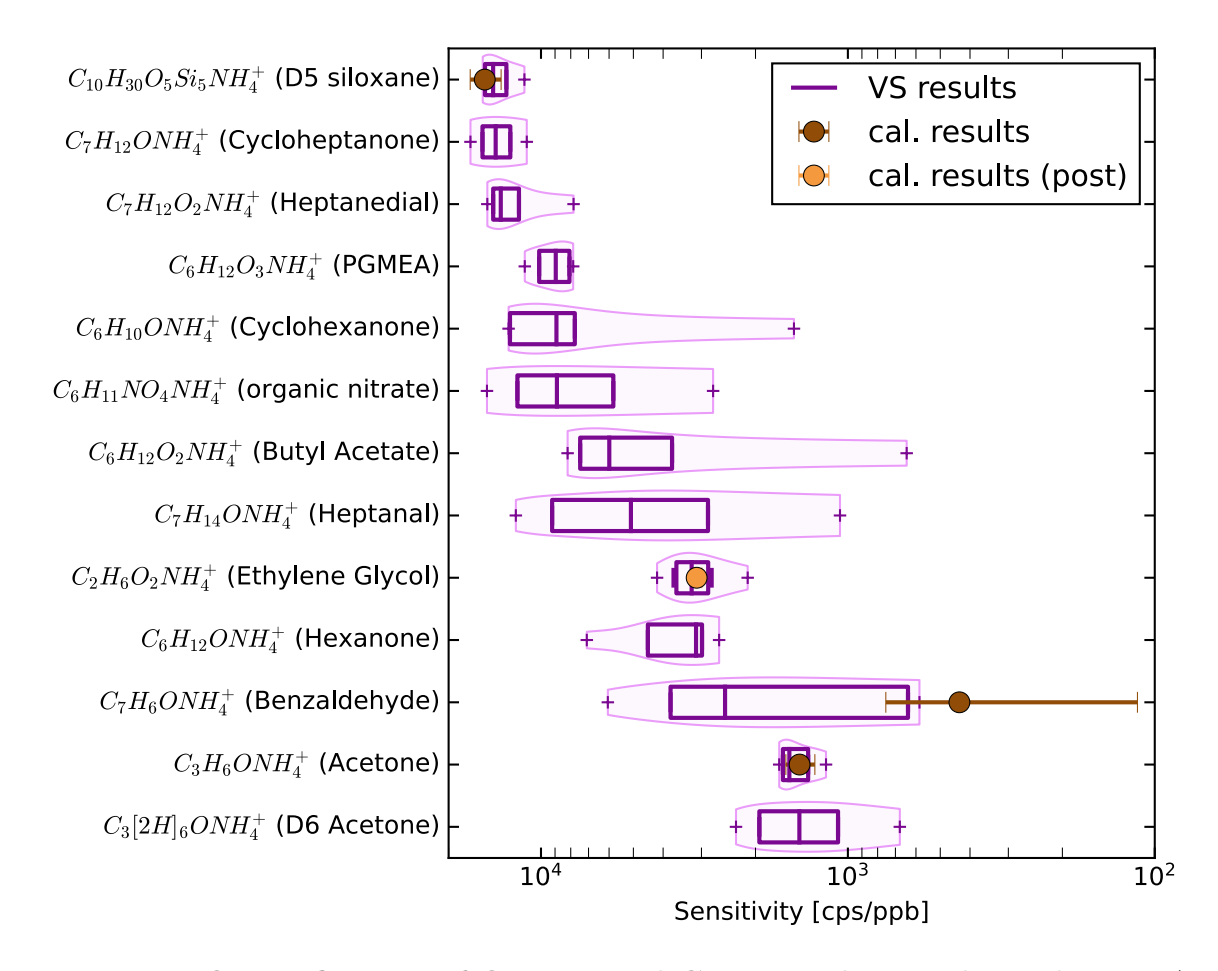


Figure 5.4.: Quantification of Oxygenated Compounds in Urban Plumes: A list of compounds relevant in urban plumes together with the internal standard D6-acetone. The names of the compounds are working titles, and it is not yet determined if these are the actual compounds measured or if they are isomers. The VS results from all ambient VS are shown in purple, with all VS longer than 7s and all fits with r² lower than 0.3 excluded. Compounds that were found in the plume periods and are part of the calibration standard have their calibration results plotted on top in brown. For ethylene glycol, a calibration result post-campaign is plotted in orange. The VS data is processed using the sigmoidal fit results (Figure 4.3). Median, upper and lower quartile re marked in the boxplots.

The quantification of additional compounds depicted in Figure 5.4 underscores the method's encouraging potential. For these compounds, calibrations have not been conducted with the instrument thus far, and for certain compounds, calibrations may not even be possible or may be very challenging. It is worth noting that all compounds detected using ammonium ionization are oxygenated and have posed challenges for detection with conventional methods like PTR MS. A comparison with literature and emission inventory values reveals that the compounds identified in this study have sources in cooking, including heptanedial, heptanal, hexanone, cyclopentanone [62], and volatile chemical products, specifically coatings and fragrances, such as D5siloxane, PGMEA, cyclohexanone, butyl acetate, ethylene glycol, and benzaldehyde [63], [19]. Given that these urban emission sources are becoming increasingly dominant in cities, it is imperative to emphasize that the VS method enables us to quantify their strength. Finally, all the above sources originate from primary emissions of anthropogenic sectors. However, during these measurements, oxidation products from these emission sources are also expected to increase. A characteristic example of urban chemistry in this context is the presence of organic nitrates, which can be extremely challenging to quantify. Here, by using the VS method we are able for the first time to constrain the sensitivity of an abundant organic nitrate in urban air with the chemical formula of $C_6H_{11}NO_4 \cdot NH_4^+$. Such quantification sets the basis for future evaluation of chemical transport models to better predict the evolution of urban plumes and the subsequent formation of secondary pollution, including ozone and aerosol particles.

6. Conclusions and Outlook

In this work, a voltage scanning technique using collision-induced-dissociation was successfully developed, optimized, and implemented in a challenging environment on-board the NASA DC-8 aircraft during the AEROMMA field campaign. The developed method facilitated the quantification of oxygenated volatile organic compounds observed in urban plumes detected during a flight over the metropolitan area of Chicago.

In preparation for the field campaign, the VOCUS chemical ionization mass spectrometer was characterized and optimized for measurements utilizing ammonium ions as reagent ions. The VS method was used to correlate signal decay rates derived from a scanning measurement to sensitivities. Decay rates were fitted using several fitting functions and optimized to capture the observed trends. The majority of compounds showed a direct decay following the ramping of voltages during the VS. However, several compounds of higher mass often showed an increase in their intensity followed by a decay. Declustering of higher-order clusters was ruled out as a relevant reason for rising signals during VS, and it was suggested that mass-dependent focusing effects might be the dominating factor in these patterns. Such decay rates were fitted using either a Gaussian function for faster batch analysis or a double sigmoidal function for targeted analysis. The latter proved to be more effective for compounds with increasing signals during VS, as indicated by the positive sigmoidal shape, offering a more accurate representation of the underlying process.

The VS method was further optimized to enhance its suitability for field campaigns. The performance of VS was assessed with a focus on concentration dependencies, particularly when employing VS at low concentrations. Furthermore, improvements were made in the VS time resolution, resulting in a reduction of VS time to just a few seconds. Overall, we found no concentration dependencies and optimal scanning conditions at an acquisition frequency of 10 Hz and a total scanning time of 5 s while scanning over a total voltage of 100 V. Such VS speeds were achieved for the first time in this work and highlight the potential of this method for field applications.

Utilization and testing in a complex field environment were achieved during the

AEROMMA campaign, where the voltage scanning method was used to quantify several compounds measured in high intensity plume periods. For the $C_2H_6O_2$ · NH_4^+ cluster (ethylene glycol) a sensitivity of $3207\pm723(23\,\%)$ cps/ppb was derived using the voltage scanning technique. This result was in great agreement with the sensitivity derived in a post campaign laboratory calibration, yielding a sensitivity of, $3110\pm119(3.8\,\%)$ cps/ppb. The quantification of additional uncalibrated OVOCs underscored the method's encouraging potential. This included the quantification of OVOCs that have sources in cooking, including heptanedial, heptanal, hexanone, and cyclopentanone, as well as in volatile chemical products, specifically coatings and fragrances, such as D5-siloxane, PGMEA, cyclohexanone, butyl acetate, ethylene glycol, and benzaldehyde. As these urban emission sources continue to gain dominance in cities, it is crucial to highlight that the VS method allows us to accurately quantify their magnitude.

Finally, we identified oxidation products originating from these emission sources, including organic nitrates, which can be exceptionally challenging to calibrate. Through the application of the VS method, we successfully determined the sensitivity of a prevalent organic nitrate in urban air for the first time, characterized by the chemical formula $C_6H_{11}NO_4 \cdot NH_4^+$. Such quantification sets the basis for future evaluation of chemical transport models enhancing our ability to forecast the development of urban plumes and the subsequent generation of secondary pollutants, such as ozone and aerosol particles.

Although comparable techniques have been tested in laboratory settings for orders of magnitude longer time resolutions, the high-speed scanning method presented in this research was an innovative approach that has considerable prospects for its practical field application in the future. Pushing the method to its limits revealed existing limitations and challenges. Continued research and resolution of these challenges may transform this method into a powerful tool for measuring uncalibratable compounds in future studies.

The methodology outlined in this work can be improved in a number of ways. One such improvement involves addressing communication issues between the instrument's software and hardware to reduce misalignment errors. By utilizing an internal standard, it may be possible to eliminate the timing offset through normalization of the starting time to a fitted function of the voltage scanning effects detected during internal standard measurement. Furthermore, a better understanding of the physical processes during voltage tuning could also lead to a more accurate interpretation

of the results. By optimizing the utilized fit function, more precise results could be achieved. A unique opportunity to differentiate between collision-induced dissociation patterns and superimposed effects could be achieved by separating the influence of declustering and possible focusing processes. However, such physical effects are not fully controlled and understood yet. Future isolation of mass and class dependent behaviors could be achieved by increasing the number of calibrated compounds measured in laboratory voltage scans. Especially intriguing for future laboratory studies will be the examination of structural isomers. If highly distinct behaviors are observed between structural isomers when undergoing voltage scans, it may be feasible to utilize this method to distinguish between various isomers during field measurements in the future.

For field applications, further analysis of data from the AEROMMA campaign and additional measurements conducted at the FZJ during the spring could facilitate the improvement of scan timing, duration, and magnitude. Improved filtering methods for low signal voltage scans are crucial in preparing the analysis method for larger-scale applications. Such low signal-to-noise periods could be excluded by automatic scripts that compare the ambient intensity relative to the background. To assess the reproducibility of the method, it is necessary to deploy the method at different measurement platforms using different instruments. Data from both ground-based campaigns and chamber experiments has been measured in Jülich and now requires evaluation.

While there are many challenges remaining, this study demonstrates the potential of the voltage scanning method for quantifying compounds in extreme field measurements. This could be a key method in the quantification of OVOCs, that can not be quantified with other calibration methods. Such refining quantification methods can foster comprehension of measured data and ultimately enhance our knowledge of observed environments. With a better understanding of the chemical evolution of VOCs and OVOCs, their formation pathways for secondary organic aerosol and ozone formation can be better understood. Therefore, this work has the potential to evaluate the contribution of currently unknown pollution sources moving a step closer to more effective mitigation strategies to address air pollution and global warming.

Bibliography

- [1] John H Seinfeld and Spyros N Pandis. *Atmospheric chemistry and physics*. 2nd ed. Nashville, TN: John Wiley & Sons, Nov. 1997.
- [2] John Houghton. "Global warming". In: Reports on Progress in Physics 68.6 (Mar. 2005), p. 1343. DOI: 10.1088/0034-4885/68/6/R02. URL: https://dx.doi.org/10.1088/0034-4885/68/6/R02.
- [3] Hannah Ritchie and Max Roser. "Urbanization". In: Our World in Data (2018). https://ourworldindata.org/urbanization.
- [4] Frank J. Kelly and Julia C. Fussell. "Air pollution and public health: emerging hazards and improved understanding of risk". In: *Environmental Geochemistry and Health* 37.4 (June 2015), pp. 631–649. DOI: 10.1007/s10653-015-9720-1. URL: https://doi.org/10.1007/s10653-015-9720-1.
- [5] Daniela Nuvolone, Davide Petri, and Fabio Voller. "The effects of ozone on human health". In: Environmental Science and Pollution Research 25.9 (May 2017), pp. 8074–8088. DOI: 10.1007/s11356-017-9239-3. URL: https://doi. org/10.1007/s11356-017-9239-3.
- [6] Ki-Hyun Kim, Ehsanul Kabir, and Shamin Kabir. "A review on the human health impact of airborne particulate matter". In: *Environment International* 74 (Jan. 2015), pp. 136–143. DOI: 10.1016/j.envint.2014.10.005. URL: https://doi.org/10.1016/j.envint.2014.10.005.
- [7] Vera Srebot et al. "Ozone and cardiovascular injury". In: Cardiovascular Ultrasound 7.1 (June 2009). DOI: 10.1186/1476-7120-7-30. URL: https://doi.org/10.1186/1476-7120-7-30.
- [8] Junfeng (Jim) Zhang, Yongjie Wei, and Zhangfu Fang. "Ozone Pollution: A Major Health Hazard Worldwide". In: Frontiers in Immunology 10 (Oct. 2019). DOI: 10.3389/fimmu.2019.02518. URL: https://doi.org/10.3389/fimmu.2019.02518.

- [9] Giuliano Polichetti et al. "Effects of particulate matter (PM10, PM2.5 and PM1) on the cardiovascular system". In: *Toxicology* 261.1-2 (June 2009), pp. 1–8. DOI: 10.1016/j.tox.2009.04.035. URL: https://doi.org/10.1016/j.tox.2009.04.035.
- [10] Benjamin A. Nault et al. "Secondary organic aerosols from anthropogenic volatile organic compounds contribute substantially to air pollution mortality". In: Atmospheric Chemistry and Physics 21.14 (July 2021), pp. 11201–11224. DOI: 10.5194/acp-21-11201-2021. URL: https://doi.org/10.5194/acp-21-11201-2021.
- [11] Kaspar R. Daellenbach et al. "Sources of particulate-matter air pollution and its oxidative potential in Europe". In: *Nature* 587.7834 (Nov. 2020), pp. 414–419. DOI: 10.1038/s41586-020-2902-8. URL: https://doi.org/10.1038/s41586-020-2902-8.
- [12] Jesse H. Kroll and John H. Seinfeld. "Chemistry of secondary organic aerosol: Formation and evolution of low-volatility organics in the atmosphere". In: Atmospheric Environment 42.16 (May 2008), pp. 3593-3624. DOI: 10.1016/j.atmosenv.2008.01.003. URL: https://doi.org/10.1016/j.atmosenv.2008.01.003.
- [13] Drew R. Gentner et al. "Review of Urban Secondary Organic Aerosol Formation from Gasoline and Diesel Motor Vehicle Emissions". In: *Environmental Science & Emp; Technology* 51.3 (Jan. 2017), pp. 1074–1093. DOI: 10.1021/acs.est.6b04509. URL: https://doi.org/10.1021/acs.est.6b04509.
- [14] Carsten Warneke et al. "Multiyear trends in volatile organic compounds in Los Angeles, California: Five decades of decreasing emissions". In: *Journal of Geophysical Research: Atmospheres* 117.D21 (Sept. 2012), n/a-n/a. DOI: 10.1029/2012jd017899. URL: https://doi.org/10.1029/2012jd017899.
- [15] Timothy Johnson and Ameya Joshi. "Review of Vehicle Engine Efficiency and Emissions". In: SAE International Journal of Engines 11.6 (2018), pp. 1307–1330. ISSN: 19463936, 19463944. URL: https://www.jstor.org/stable/26649163 (visited on 08/09/2023).
- [16] A. A. Abdel-Rahman. "On the emissions from internal-combustion engines:a review". In: *International Journal of Energy Research* 22.6 (May 1998), pp. 483–513. DOI: 10.1002/(sici)1099-114x(199805)22:6<483::aid-er377>3.0.

- co; 2-z. URL: https://doi.org/10.1002/(sici)1099-114x(199805)22: 6%3C483::aid-er377%3E3.0.co; 2-z.
- [17] HaiLin Wang et al. "Characterization and assessment of volatile organic compounds (VOCs) emissions from typical industries". In: *Chinese Science Bulletin* 58.7 (Feb. 2013), pp. 724–730. DOI: 10.1007/s11434-012-5345-2. URL: https://doi.org/10.1007/s11434-012-5345-2.
- [18] J. Kesselmeier and M. Staudt. In: Journal of Atmospheric Chemistry 33.1 (1999), pp. 23–88. DOI: 10.1023/a:1006127516791. URL: https://doi.org/ 10.1023/a:1006127516791.
- [19] Brian C. McDonald et al. "Volatile chemical products emerging as largest petrochemical source of urban organic emissions". In: *Science* 359.6377 (Feb. 2018), pp. 760–764. DOI: 10.1126/science.aaq0524. URL: https://doi.org/10.1126/science.aaq0524.
- [20] Yilin Tian et al. "Indoor emissions of total and fluorescent supermicron particles during HOMEChem". In: *Indoor Air* 31.1 (Oct. 2020), pp. 88–98. DOI: 10.1111/ina.12731. URL: https://doi.org/10.1111/ina.12731.
- [21] Peeyush Khare et al. "Asphalt-related emissions are a major missing nontraditional source of secondary organic aerosol precursors". In: Science Advances 6.36 (Sept. 2020). DOI: 10.1126/sciadv.abb9785. URL: https://doi.org/10.1126/sciadv.abb9785.
- [22] Georgios I. Gkatzelis et al. "Observations Confirm that Volatile Chemical Products Are a Major Source of Petrochemical Emissions in U.S. Cities". In: *Environmental Science & amp Technology* 55.8 (Mar. 2021), pp. 4332–4343. DOI: 10. 1021/acs.est.0c05471. URL: https://doi.org/10.1021/acs.est.0c05471.
- [23] Georgios I. Gkatzelis et al. "Identifying Volatile Chemical Product Tracer Compounds in U.S. Cities". In: *Environmental Science & Emp Technology* 55.1 (Dec. 2020), pp. 188–199. DOI: 10.1021/acs.est.0c05467. URL: https://doi.org/10.1021/acs.est.0c05467.
- [24] Matthew M. Coggon et al. "Volatile chemical product emissions enhance ozone and modulate urban chemistry". In: *Proceedings of the National Academy of Sciences* 118.32 (Aug. 2021). DOI: 10.1073/pnas.2026653118. URL: https://doi.org/10.1073/pnas.2026653118.

- [25] Alma Hodzic et al. "Characterization of organic aerosol across the global remote troposphere: a comparison of ATom measurements and global chemistry models". In: *Atmospheric Chemistry and Physics* 20.8 (Apr. 2020), pp. 4607–4635. DOI: 10.5194/acp-20-4607-2020. URL: https://doi.org/10.5194/acp-20-4607-2020.
- [26] A. Hodzic et al. "Modeling organic aerosols in a megacity: potential contribution of semi-volatile and intermediate volatility primary organic compounds to secondary organic aerosol formation". In: *Atmospheric Chemistry and Physics* 10.12 (June 2010), pp. 5491–5514. DOI: 10.5194/acp-10-5491-2010. URL: https://doi.org/10.5194/acp-10-5491-2010.
- [27] K. Dzepina et al. "Evaluation of recently-proposed secondary organic aerosol models for a case study in Mexico City". In: *Atmospheric Chemistry and Physics* 9.15 (Aug. 2009), pp. 5681–5709. DOI: 10.5194/acp-9-5681-2009. URL: https://doi.org/10.5194/acp-9-5681-2009.
- [28] C. Fountoukis et al. "Organic aerosol concentration and composition over Europe: insights from comparison of regional model predictions with aerosol mass spectrometer factor analysis". In: *Atmospheric Chemistry and Physics* 14.17 (Sept. 2014), pp. 9061–9076. DOI: 10.5194/acp-14-9061-2014. URL: https://doi.org/10.5194/acp-14-9061-2014.
- [29] H. Matsui et al. "Development of an aerosol microphysical module: Aerosol Two-dimensional bin module for foRmation and Aging Simulation (ATRAS)". In: Atmospheric Chemistry and Physics 14.18 (Sept. 2014), pp. 10315–10331. DOI: 10.5194/acp-14-10315-2014. URL: https://doi.org/10.5194/acp-14-10315-2014.
- [30] X. Zhang and J. H. Seinfeld. "A functional group oxidation model (FGOM) for SOA formation and aging". In: *Atmospheric Chemistry and Physics* 13.12 (June 2013), pp. 5907–5926. DOI: 10.5194/acp-13-5907-2013. URL: https://doi.org/10.5194/acp-13-5907-2013.
- [31] E. Athanasopoulou et al. "Modeling the meteorological and chemical effects of secondary organic aerosols during an EUCAARI campaign". In: *Atmospheric Chemistry and Physics* 13.2 (Jan. 2013), pp. 625–645. DOI: 10.5194/acp-13-625-2013. URL: https://doi.org/10.5194/acp-13-625-2013.

- [32] R. Bergström et al. "Modelling of organic aerosols over Europe (2002–2007) using a volatility basis set (VBS) framework: application of different assumptions regarding the formation of secondary organic aerosol". In: *Atmospheric Chemistry and Physics* 12.18 (Sept. 2012), pp. 8499–8527. DOI: 10.5194/acp-12-8499-2012. URL: https://doi.org/10.5194/acp-12-8499-2012.
- [33] A. P. Tsimpidi et al. "Sources and production of organic aerosol in Mexico City: insights from the combination of a chemical transport model (PMCAMx-2008) and measurements during MILAGRO". In: *Atmospheric Chemistry and Physics* 11.11 (June 2011), pp. 5153–5168. DOI: 10.5194/acp-11-5153-2011. URL: https://doi.org/10.5194/acp-11-5153-2011.
- [34] Manish K. Shrivastava et al. "Effects of gas particle partitioning and aging of primary emissions on urban and regional organic aerosol concentrations". In: Journal of Geophysical Research: Atmospheres 113.D18 (Sept. 2008). DOI: 10.1029/2007jd009735. URL: https://doi.org/10.1029/2007jd009735.
- [35] M. Shrivastava et al. "Modeling organic aerosols in a megacity: comparison of simple and complex representations of the volatility basis set approach". In: Atmospheric Chemistry and Physics 11.13 (July 2011), pp. 6639–6662. DOI: 10.5194/acp-11-6639-2011. URL: https://doi.org/10.5194/acp-11-6639-2011.
- [36] Rishabh U. Shah et al. "Urban Oxidation Flow Reactor Measurements Reveal Significant Secondary Organic Aerosol Contributions from Volatile Emissions of Emerging Importance". In: *Environmental Science & Emp Technology* 54.2 (Dec. 2019), pp. 714–725. DOI: 10.1021/acs.est.9b06531. URL: https://doi.org/10.1021/acs.est.9b06531.
- [37] Matthew C. Woody et al. "Understanding sources of organic aerosol during CalNex-2010 using the CMAQ-VBS". In: Atmospheric Chemistry and Physics 16.6 (Mar. 2016), pp. 4081-4100. DOI: 10.5194/acp-16-4081-2016. URL: https://doi.org/10.5194/acp-16-4081-2016.
- [38] J. A. de Gouw et al. "Emission and chemistry of organic carbon in the gas and aerosol phase at a sub-urban site near Mexico City in March 2006 during the MILAGRO study". In: *Atmospheric Chemistry and Physics* 9.10 (May 2009), pp. 3425–3442. DOI: 10.5194/acp-9-3425-2009. URL: https://doi.org/10.5194/acp-9-3425-2009.

- [39] Zhaofeng Tan et al. "Radical chemistry at a rural site (Wangdu) in the North China Plain: observation and model calculations of OH, HO and RO radicals". In: Atmospheric Chemistry and Physics 17.1 (Jan. 2017), pp. 663–690. DOI: 10.5194/acp-17-663-2017. URL: https://doi.org/10.5194/acp-17-663-2017.
- [40] Wen Zhang, Lu Xu, and Haofei Zhang. "Recent advances in mass spectrometry techniques for atmospheric chemistry research on molecular-level". In: Mass Spectrometry Reviews n/a.n/a (). DOI: https://doi.org/10.1002/mas.21857. URL: https://analyticalsciencejournals.onlinelibrary.wiley.com/doi/abs/10.1002/mas.21857.
- [41] Alison E Ashcroft. *Ionization methods in organic mass spectrometry*. Vol. 5. Royal Society of Chemistry, 1997.
- [42] Tilmann D Märk and Gordon H Dunn. *Electron impact ionization*. Springer Science & Business Media, 2013.
- [43] Hanan Awad, Mona M Khamis, and Anas El-Aneed. "Mass spectrometry, review of the basics: ionization". In: *Applied Spectroscopy Reviews* 50.2 (2015), pp. 158–175.
- [44] Gary L Glish and Richard W Vachet. "The basics of mass spectrometry in the twenty-first century". In: *Nature reviews drug discovery* 2.2 (2003), pp. 140–150.
- [45] Ulrich Boesl. "Time-of-flight mass spectrometry: introduction to the basics". In: Mass spectrometry reviews 36.1 (2017), pp. 86–109.
- [46] Robert S Blake et al. "Chemical ionization reaction time-of-flight mass spectrometry: Multi-reagent analysis for determination of trace gas composition". In: *International Journal of Mass Spectrometry* 254.1-2 (2006), pp. 85–93.
- [47] Robert S Blake, Paul S Monks, and Andrew M Ellis. "Proton-transfer reaction mass spectrometry". In: *Chemical reviews* 109.3 (2009), pp. 861–896.
- [48] Markus Müller et al. "A novel method for producing NH4+ reagent ions in the hollow cathode glow discharge ion source of PTR-MS instruments". In: International Journal of Mass Spectrometry 447 (2020), p. 116254.
- [49] Eva Canaval et al. "NH 4+ association and proton transfer reactions with a series of organic molecules". In: Frontiers in Chemistry 7 (2019), p. 191.

- [50] Lu Xu et al. "A Chemical Ionization Mass Spectrometry Utilizing Ammonium Ions (NH₄⁺ CIMS) for Measurements of Organic Compounds in the Atmosphere". In: (Aug. 2022). DOI: 10.5194/amt-2022-228.
- [51] Jordan Krechmer et al. "Evaluation of a New Reagent-Ion Source and Focusing Ion-Molecule Reactor for Use in Proton-Transfer-Reaction Mass Spectrometry". In: Analytical Chemistry 90.20 (Sept. 2018), pp. 12011-12018. DOI: 10.1021/acs.analchem.8b02641. URL: https://doi.org/10.1021/acs.analchem. 8b02641.
- [52] Martin Breitenlechner et al. "PTR3: An Instrument for Studying the Lifecycle of Reactive Organic Carbon in the Atmosphere". In: *Analytical Chemistry* 89.11 (May 2017), pp. 5824–5831. DOI: 10.1021/acs.analchem.6b05110. URL: https://doi.org/10.1021/acs.analchem.6b05110.
- [53] TOFWERK. TOFWERK landing page. 2023. URL: https://www.tofwerk.com/ (visited on 08/28/2023).
- [54] Aerodyne Research. Aerodyne Research landing page. 2023. URL: https://www.aerodyne.com/ (visited on 11/01/2023).
- [55] A. Zaytsev et al. "Using collision-induced dissociation to constrain sensitivity of ammonia chemical ionization mass spectrometry (NH₄⁺ CIMS) to oxygenated volatile organic compounds". In: Atmospheric Measurement Techniques 12.3 (2019), pp. 1861–1870. DOI: 10.5194/amt-12-1861-2019. URL: https://amt.copernicus.org/articles/12/1861/2019/.
- [56] M. McFarland et al. "Flow-drift technique for ion mobility and ion-molecule reaction rate constant measurements. II. Positive ion reactions of N+, O+, and H2+ with O2 and O+ with N2 from thermal to [inverted lazy s]2 eV". In: *The Journal of Chemical Physics* 59.12 (Dec. 1973), pp. 6620–6628. DOI: 10.1063/1.1680042. URL: https://doi.org/10.1063/1.1680042.
- [57] Gregory H. Wannier. "Motion of gaseous ions in strong electric fields". In: *The Bell System Technical Journal* 32.1 (1953), pp. 170–254. DOI: 10.1002/j.1538-7305.1953.tb01426.x.
- [58] Gerhard Steiner et al. "High-Resolution Mobility and Mass Spectrometry of Negative Ions Produced in a ²⁴¹Am Aerosol Charger". In: Aerosol Science and Technology 48.3 (Jan. 2014), pp. 261–270. DOI: 10.1080/02786826. 2013.870327. URL: https://doi.org/10.1080/02786826.2013.870327.

- [59] Carlos Larriba et al. "The mobility-volume relationship below 3.0 nm examined by tandem mobility-mass measurement". In: Aerosol Science and Technology 45.4 (2011), pp. 453–467.
- [60] Bon Ki Ku and Juan Fernandez De La Mora. "Relation between electrical mobility, mass, and size for nanodrops 1–6.5 nm in diameter in air". In: *Aerosol Science and Technology* 43.3 (2009), pp. 241–249.
- [61] WD Kilpatrick. "An experimental mass-mobility relation for ions in air at atmospheric pressure". In: *Proc. Annu. Conf. Massspectrosc.* Vol. 19. 1971, pp. 320–325.
- [62] Felix Klein et al. "Characterization of Gas-Phase Organics Using Proton Transfer Reaction Time-of-Flight Mass Spectrometry: Cooking Emissions". In: *Environmental Science & Eamp Technology* 50.3 (Jan. 2016), pp. 1243–1250. DOI: 10. 1021/acs.est.5b04618. URL: https://doi.org/10.1021/acs.est.5b04618.
- [63] Peeyush Khare et al. "Ammonium adduct chemical ionization to investigate anthropogenic oxygenated gas-phase organic compounds in urban air". In: *Atmospheric Chemistry and Physics* 22.21 (Nov. 2022), pp. 14377–14399. DOI: 10.5194/acp-22-14377-2022. URL: https://doi.org/10.5194/acp-22-14377-2022.
- [64] Paolo Cianconi et al. "Human Responses and Adaptation in a Changing Climate: A Framework Integrating Biological, Psychological, and Behavioural Aspects". In: *Life* 11.9 (2021). ISSN: 2075-1729. URL: https://www.mdpi.com/2075-1729/11/9/895.
- [65] Gelsomina Pappalardo. "ACTRIS Aerosol, Clouds and Trace Gases Research Infrastructure". In: *EPJ Web of Conferences* 176 (2018). Ed. by D. Nicolae et al., p. 09004. DOI: 10.1051/epjconf/201817609004. URL: https://doi.org/10.1051/epjconf/201817609004.
- [66] Qu Liang et al. "Imaging VOC distribution in cities and tracing VOC emission sources with a novel mobile proton transfer reaction mass spectrometer". In: *Environmental Pollution* 265 (2020), p. 114628.
- [67] Ralf Tillmann et al. "Air quality observations onboard commercial and targeted Zeppelin flights in Germany–a platform for high-resolution trace-gas and aerosol measurements within the planetary boundary layer". In: Atmospheric Measurement Techniques 15.12 (2022), pp. 3827–3842.

- [68] Mathew R Heal, Prashant Kumar, and Roy M Harrison. "Particles, air quality, policy and health". In: *Chemical Society Reviews* 41.19 (2012), pp. 6606–6630.
- [69] United States Environmental Protection Ageny. particulate-matter-pm25-trends. 2022. URL: https://www.epa.gov/air-trends/particulate-matter-pm25-trends (visited on 10/25/2023).
- [70] Lutz Bretschneider et al. "MesSBAR—Multicopter and Instrumentation for Air Quality Research". In: *Atmosphere* 13.4 (Apr. 2022), p. 629. DOI: 10.3390/atmos13040629. URL: https://doi.org/10.3390/atmos13040629.
- [71] National Oceanic and Atmospheric Administration U.S. Department of Commerce. AEROMMA: Investigation atmospheric emissions and chemical reactions that affect air quality and climate. 2023. URL: https://csl.noaa.gov/projects/aeromma/ (visited on 08/29/2023).
- [72] Julia Jäger. Airborne VOC measurements on board the Zeppelin NT during the PEGASOS campaigns in 2012 deploying the improved Fast-GC-MSD System. Forschungszentrum Jülich, 2014.
- [73] F. Pedregosa et al. "Scikit-learn: Machine Learning in Python". In: *Journal of Machine Learning Research* 12 (2011), pp. 2825–2830.

A. Appendix

A.1. Instrument Background

High background signals reduce the quality of the measured data. Fluctuating and highly variable backgrounds pose challenges to analyzing and interpreting data. In cases where the signal-to-noise ratio is reduced, signals may not be sufficiently separated from the background. Additionally, elevated background levels restrict the extent to which signal enhancements can occur. It is therefore essential to take measures to reduce the instrument's background.

High purity of zero air gases is crucial in precisely determining background interferences. The liquid solutions of NH₃ and H₂O, along with the zero air and calibration standard, should have minimal contamination. Nevertheless, as the NH₃ solution ages, replacing the solution leads to the contamination of the instrument lines because of its exposure to ambient air. Subsequently, it takes a considerable amount of time for the VOCUS system to reach again equilibrium. To reduce the risk of contamination or leakage a pump is introduced into the line between the NH₃ solution and the mass flow controller that is used to regulate the flow into the ion source. After changing the solution or periods of inactivity, the line can be pumped to pump out the ambient contaminated air.

Instrument backgrounds tend to decrease when the instrument operates for extended durations. To minimize the downtime and maintain a continuous vacuum, shutting down the instrument is avoided whenever possible. This approach helps reduce the effects of potential leaks and the accumulation of deposits inside the instrument.

An essential part of the regular maintenance procedures for the instrument involves tuning the detector. Over time, the MCP elements within the detector degrade, leading to a reduced performance. Regular retuning of the voltages is crucial to ensure that the signals maintain their strength. Failure to tune the detector correctly can result in detector noise, which influences the signal-to-noise ratio and therefore

increases the uncertainties of background corrections.

Finally, on all instrument parts, and particularly on the ion source, leakage is a significant cause of high background signals. Intensive and regular leak testing is essential for ensuring optimal instrument performance.

A.2. Instrument Comparison

In Xu et al. [50] the fractional contribution of different ionization pathways for the detection of species contained in calibration gas standards are discussed (see calibration gas details in Appendix A.3) and compared to this work. The high sensitivity and dominant contribution of NH_4^+ ionization is observed by Lu et al. as well as in this work, with MVK, acetone, and pentanone. For aldehydes, acetaldehyde and pentanal/pentanone show a similar ionization scheme and for both instruments share medium sensitivity. High \mathbf{H}^+ ionization contribution is observed for both instruments for a common monoterpene, α -pinene, as well as alkenes. In addition, both instruments show similar sensitivity for α -pinene. With no shared alcohols in the calibration standards and a high variability observed in the sensitivities of different calibrated alcohols, a comparison is difficult. For alcohols, both instruments show mostly lower sensitivities and mostly low contribution by NH_4^+ ionization. For aromatics, specifically toluene and xylene, both instruments show a dominant \mathbf{H}^+ ionization and very low overall sensitivity. In conclusion, both instruments exhibit similar performance, providing confidence that findings and conclusions regarding the operation of one instrument can be extrapolated to guide the optimal operation of the other.

A.3. Calibration results

Name	Formula	Mass	Av. Sensitivity	Cal. Bottle
		[amu]	[ncps/ppb]	[ppb]
Nopinone	$C_9H_{14}O$	138.10	$1.95\text{E-}01 \pm 1.34\text{E-}02$	848.22 ± 72.21
Pentan-3-one	$C_5H_{10}O$	86.07	$1.47E-01 \pm 3.59E-03$	1141.81 ± 97.21
Butan-2-one	C_4H_8O	72.06	$1.05E-01 \pm 1.89E-03$	1363.89 ± 116.11
MVK	C_4H_6O	70.04	$8.03\text{E}-02 \pm 1.97\text{E}-03$	1404.88 ± 119.6
Acetone	C_3H_6O	58.04	$6.39\text{E-}02 \pm 1.11\text{E-}03$	1659.73 ± 141.3
Acetonitrile	C_2H_3N	41.03	$3.36E-02 \pm 1.78E-03$	2334.87 ± 198.78
a-Pinene	$C_{10}H_{16}$	136.13	$2.09E-02 \pm 1.23E-03$	752.65 ± 64.08
Butan-1-ol	$C_4H_{10}O$	74.07	$5.13\text{E-}03 \pm 2.56\text{E-}04$	1332.61 ± 113.45
Isoprene	C_5H_8	68.06	$5.76E-04 \pm 5.68E-06$	1219.06 ± 103.78
Acetaldehyde	C_2H_4O	44.03	$2.06E-04 \pm 4.33E-05$	2148.45 ± 182.91
Benzene	C_6H_6	78.05	$2.15E-05 \pm 5.62E-06$	1372.18 ± 116.82
Toluene	C_7H_8	92.06	$9.26E-06 \pm 1.47E-06$	1146.6 ± 97.62
Methanol	CH ₄ O	32.03	$6.33\text{E-}06 \pm 9.45\text{E-}07$	3008 ± 256.09
Xylene	C_8H_{10}	106.08	$4.83E-06 \pm 1.13E-06$	960.1 ± 81.74
Chlorobenze	C_6H_5Cl	112.01	$-1.31E-05 \pm 8.20E-05$	1200.87 ± 102.24

Table A.1.: Calibration Results for the FZJ VOCUS: Results from Calibrations performed during a 3-week period in spring 2023.

Name	Formula	Mass	Av. Sensitivity
		[amu]	[cps/ppb]
D5-Siloxane	$C_{10}H_{30}O_5Si_5$	370.09	15249±1761
Benzonitrile	C_7H_5N	103.04	4519±187
MVK	C_4H_6O	70.04	2103±228
Acetone	C_3H_6O	58.04	1437±156
Acetonitrile	C_2H_3N	41.03	839±110
Acrolein	C_3H_4O	56.03	269±41
Acetaldehyde	C_2H_4O	44.03	26±5
Methacrolein	C4H6O	70.04	514±25
Isoprene	C_5H_8	68.06	27±5
Styrene	C8H8	104.06	348 ± 30

Table A.2.: Calibration Results from the NOAA VOCUS: Results from Calibrations performed in the second period of the AEROMMA campaign.

A.4. Error Propagation of Conversion to Kinetic Energie

In the following, the error propagation for the formula derived in 4.2.1 is presented. Error for a, b, and c were not stated in Steiner et al. [58]. To emphasize the impact of these errors, the error propagation is also performed for Z_0 .

$$\Delta < \mathbf{E_{kin}^{cm}} > = \left(\left(\Delta Z \frac{\partial < \mathbf{E_{kin}^{cm}} >}{\partial Z} \right)^{2} + \left(\Delta \mathbf{U} \frac{\partial < \mathbf{E_{kin}^{cm}} >}{\partial \mathbf{U}} \right)^{2} + \left(\Delta d \frac{\partial < \mathbf{E_{kin}^{cm}} >}{\partial d} \right)^{2} + \left(\Delta T \frac{\partial < \mathbf{E_{kin}^{cm}} >}{\partial T} \right)^{2} \right)^{\frac{1}{2}}$$
(A.1)

$$\frac{\partial \langle \mathbf{E_{kin}^{cm}} \rangle}{\partial Z} = \frac{m_a}{m_a + m_r} \left(\frac{1}{2} Z \left(\frac{\mathbf{U}}{d} \right)^2 (m_r + m_b) \right) \tag{A.2}$$

$$\frac{\partial \langle \mathbf{E_{kin}^{cm}} \rangle}{\partial \mathbf{U}} = \frac{m_a}{m_a + m_r} \left(\frac{1}{2} \mathbf{U} \left(\frac{Z}{d} \right)^2 (m_r + m_b) \right)$$
(A.3)

$$\frac{\partial \langle \mathbf{E_{kin}^{cm}} \rangle}{\partial d} = \frac{m_a}{m_a + m_r} \left(\frac{1}{2} \left(-\frac{1}{d^2} \right) (Z \cdot \mathbf{U})^2 (m_r + m_b) \right) \tag{A.4}$$

$$\frac{\partial \langle \mathbf{E_{kin}^{cm}} \rangle}{\partial T} = \frac{3}{2} k_B \tag{A.5}$$

$$\Delta Z = \left(\left(\Delta Z_0 \frac{1013 \, mbar}{p} \frac{T}{273 \, K} \right)^2 + \left(-\Delta p \cdot Z_0 \frac{1013 \, mbar}{p^2} \frac{T}{273 \, K} \right)^2 + \left(\Delta T \cdot Z_0 \frac{1013 \, mbar}{p} \frac{1}{273 \, K} \right)^2 \right)^{\frac{1}{2}} \tag{A.6}$$

$$\Delta Z_0 = \left(\left(\Delta a \left(m_r + m_a \right)^b \right)^2 + \left(\Delta b \cdot \frac{a}{b} \left(m_r + m_a \right)^{b-1} \right)^2 + \left(\Delta c \right)^2 \right)^{\frac{1}{2}}$$
 (A.7)

A.5. Lag of written Voltage Values

Figure A.1 displays data extracted from the data files of the NOAA VOCUS during the AEROMMA flight over Chicago to show the potential risks associated with misalignment resulting from data mismatching based on the written indicators of the VS scripting. The first example shows the ambient VS 7, which was overestimating the ΔE_{kin}^{50} . This occurred because the parameter "VS Scripting" was marked as active much earlier in the data than when the actual effect of the VS began. It is evident that the voltages recorded in the data files for both the set point and the read-back value lag behind and exhibit unpredictable jumps. The VS scripting implements the voltage changes in much smaller steps than they are written in the files. The read-back value is not particularly useful as it jumps to a maximum value that does not reflect the set maximum value and lacks objectivity. Even for the good performing VS, ambient VS 17, the read back is lagging far behind. It is evident that these effects vary in each run, and the assumption is that the recorded values do not update quickly or accurately enough. In both examples illustrated above, the VS should have completed within 5 s, but both examples show a clear lag of varying magnitude.

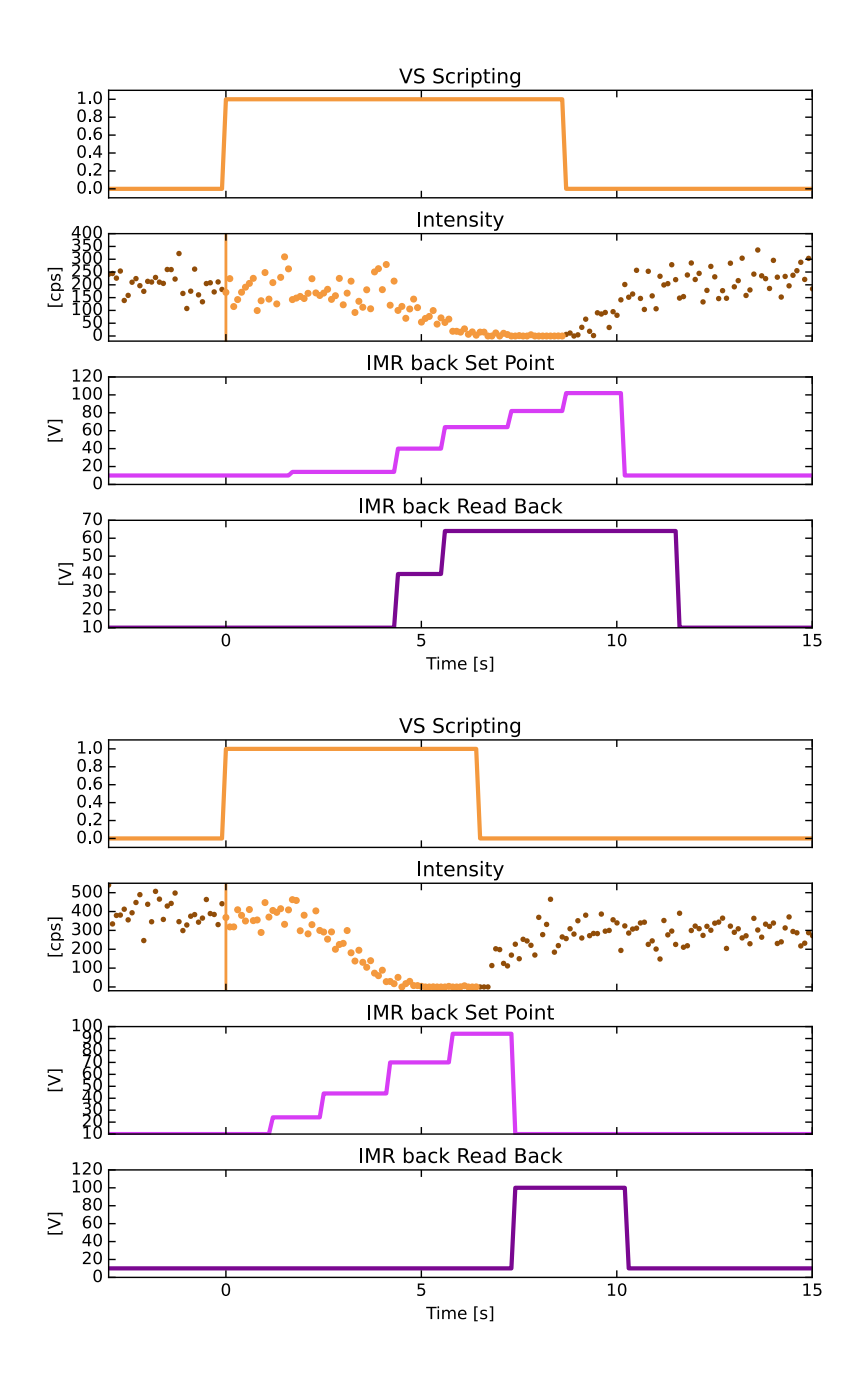


Figure A.1.: Written Instrument Parameters during VS: VS 7 (top) as a good and VS 17 (bottom) as a bad example of VS data alignment from measurements of the AEROMMA Chicago flight for $C_2H_6O_2\cdot NH_4^+$. The VS Scripting indicates if the scripting is active, the time series of $C_2H_6O_2\cdot NH_4^+$ highlights the chosen periods for the VS processing marked in orange, and the IMR back set point and read-back parameters as written in the measurements instrument data are presented against the time relative to the indicated start of the VS.

A.6. Calculation of Coefficient of Determination for fitted Data

For evaluation of fits performed in this work, the coefficient of determination or r^2 score is used. This is implemented in Python with the package skikit-learn [73]. The r^2 score gives a ratio of variation. Independent variables are parameters used in the fit function. The dependable variable is the result of the fit. The r^2 score can be 1.0 or lower. With 1.0 describing a fit where all data points are described perfectly by the independent variables. In equation A.8 y_i is the input data point, while \hat{y}_i is the value predicted by the fit for the given data point. \bar{y} is the average value of the input data.

$$r^{2}(y,\hat{y}) = 1 - \frac{\sum_{i=1}^{n} (y_{i} - \hat{y}_{i})^{2}}{\sum_{i=1}^{n} (y_{i} - \bar{y})^{2}}$$
(A.8)

The r^2 score used in this work is not a simple linear regression score, which is often referred to as r^2 . While the coefficient of determination is commonly denoted as R^2 , it is not in this work. Instead, r^2 is used to denote the coefficient of determination, as explained here and further described in [73].

A.7. Using squared Voltage instead of Kinetic Energies

The conversion into kinetic energies presented by Zaytsev et al. [55] and widely used so far in the field has high uncertainties and low physical accuracy. Since the ion mobility scales quadratic in the conversion, so do the empirically determined constants commonly used. These constants have been fitted on a dataset that is rather poor in the lower mass range. To avoid these uncertainties and to significantly simplify the VS processing, an alternative is presented. This makes it proportional to the applied field energy in $W = \frac{V^2}{\Omega}$.

In Figure A.2 data is presented that was calculated from a calibration voltage scanning measurement with a VOC calibration gas bottle. The dataset was converted into both $\rm U^2$ and kinetic energies and then processed to generate the $\Delta \rm U^2{}_{50}$ and $\Delta \rm E^{50}_{kin}$ values using a gauss fit. When these values are compared directly, a high linear correlation is found ($\rm r^2=0.986$). These results promote that instead of converting the applied voltages of the VS into kinetic energies, as described in 4.2.1, it is suggested, that keeping the voltages as the basis for further calculations would be sufficient. While this would lose some physicality and information regarding the

examined system, the simplified approach would yield almost the same results with highly reduced computational times.

Still, there is a minor mass dependency in the conversion to kinetic energies, which is noticeable in the comparison. Although this could be a good way to apply the voltage

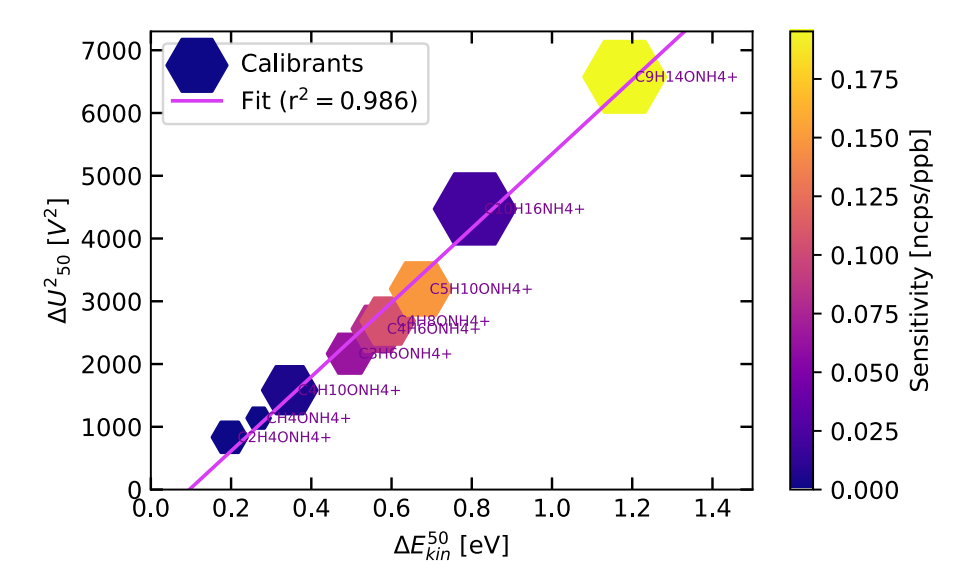


Figure A.2.: Comparison between ΔU^2_{50} and ΔE^{50}_{kin} : calibration data processed using both conversion to ΔE_{kin} and ΔU^2 . A linear fit is applied. The data points are colored by the sensitivity derived from a step calibration, and the size of the data points reflects the mass of the clusters.

scanning method in the future and reduce the development and processing time, this work uses data converted into kinetic energies. This ensures, that the physical interpretation of the absolute energy values remains possible for future investigations and ensures a coherency with the referenced literature.

A.8. Effect of Data Misalignment

To visualize the distortion of the VS processing due to data misalignment, the calculated ΔE_{kin}^{50} values of the ethylene glycol time series of the AEROMMA Chicago flight are presented in Figure A.3. With the VS scripting set to tune over 100 V in 5 s, all VS measurements show a lag of at least 1 s in the written indicator. With longer lags, the calculated ΔE_{kin}^{50} values increase.

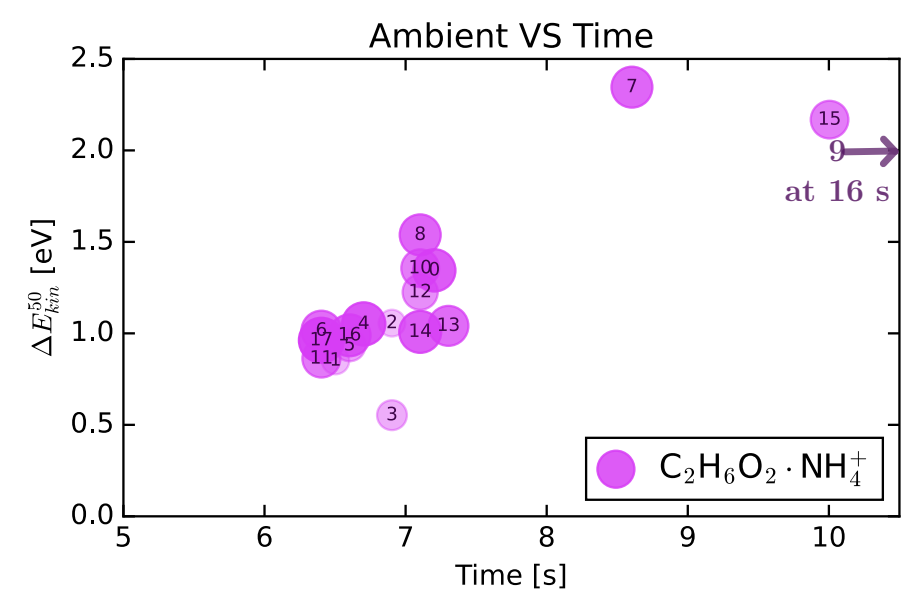


Figure A.3.: Shifting of the calculated ΔE_{kin}^{50} values due to misalignment of data: Ambient VS results of the AEROMMA Chicago flight for $C_2H_6O_2\cdot NH_4^+$. The VS number is written on the marker and the marker size scales with the r^2 value of the VS fit indicating the quality of the fit.

A.9. Ethylene Glycol VS results

Nr.	$\Delta { m E_{kin}^{50}}$	$\mathbf{r^2}$	Duration	av. Int. before	av. Int. after	Int. change
	[eV]		[s]	[cps]	[cps]	[cps/s]
0	1.34	0.85	7.20	212 (±40)	168 (±40)	$-1.96 (\pm 2.55)$
1	0.85	0.36	6.50	23 (±17)	24 (±17)	0.04 (±1.09)
2	1.06	0.34	6.90	22 (±16)	21 (±17)	-0.05 (±1.06)
3	0.55	0.42	6.90	30 (±22)	34 (±22)	$0.16 (\pm 1.40)$
4	1.05	0.88	6.70	$280 \ (\pm 69)$	$275 (\pm 69)$	-0.20 (±4.51)
5	0.93	0.48	6.60	$35 (\pm 23)$	$42\ (\pm 23)$	$0.30 (\pm 1.48)$
6	1.01	0.75	6.40	140 (±41)	128 (±41)	$-0.56 (\pm 2.69)$
7	2.35	0.79	8.60	$200 (\pm 59)$	$163 (\pm 59)$	$-1.57 (\pm 3.55)$
8	1.54	0.79	7.10	101 (±37)	116 (±37)	$0.71 (\pm 2.36)$
9	2.00	0.51	16.01	$177 (\pm 30)$	$86 \ (\pm 30)$	-2.93 (±1.39)
10	1.36	0.68	7.10	117 (±23)	49 (±23)	$-3.05 (\pm 1.50)$
11	0.86	0.68	6.40	88 (±32)	$97 (\pm 32)$	$0.43 (\pm 2.10)$
12	1.23	0.58	7.10	$50 \ (\pm 25)$	$42\ (\pm 25)$	$-0.33 (\pm 1.60)$
13	1.04	0.75	7.30	98 (±33)	109 (±33)	$0.49 (\pm 2.08)$
14	1.01	0.83	7.10	94 (±32)	119 (±32)	$1.10 (\pm 2.04)$
15	2.17	0.67	10.00	71 (±26)	$59 \ (\pm 26)$	-0.48 (±1.48)
16	0.99	0.83	6.60	81 (±34)	$77 (\pm 34)$	$-0.20 (\pm 2.22)$
17	0.96	0.96	6.40	415 (±65)	$302 (\pm 65)$	-5.28 (±4.28)

Table A.3.: Results of $C_2H_6O_2$ · NH_4^+ Ambient VS measurements: Derived ΔE_{kin}^{50} and corresponding r^2 values, as well as the total written duration of the VS and the average intensity before and after the VS and the resulting intensity change during the VS.

Nr.	$\Delta { m E_{kin}^{50}}$	\mathbf{r}^{2}	Duration	av. Int. before	av. Int. after	Int. change
	[eV]		[s]	[cps]	[cps]	[cps/s]
0	1.29	0.34	7.50	26 (±21)	27 (±21)	$0.06 (\pm 1.32)$
1	0.93	0.56	6.90	31 (±25)	$32\ (\pm 25)$	$0.07 (\pm 1.59)$
2	0.41	0.59	7.00	34 (±20)	$28 \ (\pm 20)$	-0.24 (±1.26)
3	2.10	0.45	7.10	26 (±19)	24 (±19)	-0.08 (±1.20)

Table A.4.: Results of $C_2H_6O_2$ · NH_4^+ Calibration and Zero VS measurements: Derived ΔE_{kin}^{50} and corresponding r^2 values, as well as the total written duration of the VS and the average Intensity before and after the VS and the resulting intensity change during the VS.

A.10. Plume Compounds

Name	Formula	Mass	mean VS. Sens	mean Cal. Sens
(possible)		[amu]	[cps/ppb]	[cps/ppb]
D5-Siloxane	$C_{10}H_{30}O_5Si_5$	370.09	13863 ± 1899	15249 ± 1761
Cycloheptanone	$C_7H_{12}O$	112.09	14051 ± 4138	
Heptanedial	$C_7H_{12}O_2$	128.08	12485 ± 2858	
PGMEA	$C_6H_{12}O_3$	132.08	9262 ± 1590	
Cyclohexanone	$C_6H_{10}O$	98.07	8707 ± 4599	
Org. Nitrate	$C_6H_{11}NO_4$	161.07	8874 ± 8662	
Butyl Acetate	$C_6H_{12}O_2$	116.08	5203 ± 3362	
Heptanal	$C_7H_{12}O_2$	128.08	6057 ± 4534	
Ethylene Glycol	$C_2H_6O_2$	62.04	3207 ± 723	
Hexanone	$C_6H_{12}O$	100.09	4063 ± 1834	
Benzaldehyde	C_7H_6O	106.04	2715 ± 2302	433 ± 319
Acetone	C_3H_6O	58.04	1476 ± 208	1437 ± 156
D6-Acetone	$C_{3}[2H]_{6}O$	64.08	1490 ± 656	

Table A.5.: Possible Plume Compounds and Internal Standard: Results from Voltage Scans performed on the first Chicago flight of the AEROMMA campaign and calibrations performed during the second period of AEROMMA. Values displayed here are not median values as in Figure 5.4, but averages with standard deviations as errors. VS results from VS with durations longer 7s and from VS with r² scores lower than 0.3 as well as the low signal VS 0,1,2,3 are excluded.

B. Utilized Software

For operation of the FZJ VOCUS, software provided by TOFWERK was used. in particular "Acquility" and "TofDaq" for running measurement and "TOFWARE" for analyzing, baseline correcting, and peak fitting the measured data. The NOAA VOCUS was operated using "LabVIEW".

Further coding for data analysis and plotting was done in this work using "Python", and the packages, "pandas", "numpy", "matplotlib", "h5py", "os", "math", "sklearn", "datetime", "scipy", "molmass" and "cartopy". Additionally, "Igor" was used for processing and plotting calibration data. Vector graphics were created using "Inkscape". "ifftex" was used for writing the thesis. For spell checking and improvement of grammar and readability, "DeepL", "LanguageTool" and "ChatGPT" were utilized on a word or sentence scale. "ChatGPT" was also used to generate short code snippets to assist in the writing of Python code.

C. Acknowledgments

Astrid Kiendler-Scharr's teaching and passion for science was truly inspiring. May her legacy help to shape a better world.

I want to extend my gratitude to Prof. Dr. Hendrik Fuchs for his supervision, encouragement, support, and trust. Furthermore, I thank my second examiner, Prof. Dr. Stephan Schlemmer, for taking the time to also be part of this final chapter of my masters studies. I extend my heartfelt gratitude to my supervisor Dr. Georgios Gkatzelis for his unwavering enthusiasm, invaluable support, and encouragement throughout this project. His passion for the subject and constant guidance made this journey truly enjoyable and fulfilling.

Thanks to the entire "Organic Trace Gases" team for their pleasant collaboration, their input, and assistance. Special thanks to Sergej Wedel and Dr. Hariprasad Dilipkumar Alwe for their invaluable assistance and expertise in operating the VOCUS instrument. Thanks to Dr. Hui Wang for the insightful discussions about voltage scanning and cooking emissions. Many thanks to the whole NOAA team for giving me the opportunity to join the AEROMMA campaign and test the VS method.

I am grateful to my family for their unfailing support throughout my studies. This accomplishment would not have been possible without their immense encouragement and assistance. Thanks to the Thorsties who accompanied me throughout my studies and with whom I shared many cups of coffee, insightful discussions, and good times. Finally, I would like to thank my partner Dina, who has always been by my side and had my back at all times.

This work has been made possible by funding of the Klaus Tschira Boost Fund, a joint initiative of the German Scholars Organization and the Klaus Tschira Stiftung.

D. Selbstständigkeitserklärung

Hiermit versichere ich an Eides statt, dass ich die vorliegende Arbeit selbstständig und ohne die Benutzung anderer als der angegebenen Hilfsmittel angefertigt habe. Alle Stellen, die wörtlich oder sinngemäß aus veröffentlichten und nicht veröffentlichten fremden Schriften entnommen wurden, sind als solche kenntlich gemacht. Die Arbeit ist in gleicher oder ähnlicher Form im Rahmen einer anderen Prüfung noch nicht vorgelegt worden.

Milan Roska

